

BIELEFELD UNIVERSITY

MASTER THESIS

---

**The canonical phase diagram in strong  
coupling lattice QCD from the  
Wang-Landau method**

---

*Author:*  
Aaron VON KAMEN

*Supervisor:*  
Dr. Wolfgang UNGER

*Second supervisor:*  
Prof. Dr. Owe PHILIPSEN

*A thesis submitted in fulfillment of the requirements  
for the degree of Master in mathematical and theoretical Physics*

*in the group for*

Numerical simulations and field theory on the lattice  
High Energy Physics

July 22, 2019



## Declaration of Authorship

I, Aaron VON KAMEN, declare that this thesis titled, "The canonical phase diagram in strong coupling lattice QCD from the Wang-Landau method" and the work presented in it are my own. I confirm that:

- This work was done wholly or mainly while in candidature for a research degree at this University.
- Where any part of this thesis has previously been submitted for a degree or any other qualification at this University or any other institution, this has been clearly stated.
- Where I have consulted the published work of others, this is always clearly attributed.
- Where I have quoted from the work of others, the source is always given. With the exception of such quotations, this thesis is entirely my own work.
- I have acknowledged all main sources of help.
- Where the thesis is based on work done by myself jointly with others, I have made clear exactly what was done by others and what I have contributed myself.

Signed:

---

Date:

---



BIELEFELD UNIVERSITY

# *Abstract*

Physics Faculty  
High Energy Physics

Master in mathematical and theoretical Physics

**The canonical phase diagram in strong coupling lattice QCD from the  
Wang-Landau method**

by Aaron VON KAMEN

**In this thesis the Wang-Landau method is established in the continuous time limit of strong coupling lattice QCD. With this method at hand, we generate the canonical density of states (DoS). In addition to calculating the expectation values of observables, we use the canonical DoS to determine the phase boundary at the first order transition between the low density and high density phase. We study both the grand canonical  $T - \mu_B$  and canonical  $T - n_B$  phase diagram for the  $SU(3)$  gauge group. We find that our continuous time phase boundary results are representative for the phase boundaries of a discrete time system which also involves dynamic baryons.**



## *Acknowledgements*

Numerical simulations were performed on the OCuLUS cluster (Paderborn University). I acknowledge my supervisor Wolfgang Unger for his good mentoring and advice I received throughout my thesis.



# Contents

<b>Declaration of Authorship</b>	<b>iii</b>
<b>Abstract</b>	<b>v</b>
<b>Acknowledgements</b>	<b>vii</b>
<b>Motivation</b>	<b>1</b>
<b>1 Introduction to Quantum Chromodynamics</b>	<b>3</b>
1.1 Fermions in QCD . . . . .	3
1.2 Gauge symmetry . . . . .	4
<b>2 Lattice Quantum Chromodynamics</b>	<b>5</b>
2.1 The path integral formalism . . . . .	5
2.2 Discretization of fermions . . . . .	6
2.3 Staggered fermions . . . . .	8
2.4 Temperature in lattice QCD . . . . .	8
2.5 The chemical potential in lattice QCD . . . . .	9
<b>3 Strong coupling lattice QCD at finite baryon-number density</b>	<b>11</b>
3.1 The monomer, dimer and polymer model . . . . .	11
3.2 The sign . . . . .	14
3.3 The continuous time limit . . . . .	14
3.3.1 $\gamma$ and $N_\tau$ large . . . . .	15
3.3.2 The $N_\tau \rightarrow \infty$ & $\gamma \rightarrow \infty$ limits . . . . .	17
<b>4 Methods</b>	<b>21</b>
4.1 The microcanonical density of states from the Wang-Landau method . . . . .	21
4.2 The Wang-Landau algorithm applied to the Ising model . . . . .	23
4.3 Finite-Size Scaling . . . . .	26
4.4 Finite-Size scaling applied to the Ising model . . . . .	26
4.5 The worm algorithm in SC-QCD . . . . .	29
4.6 Worm algorithm in CT-limit . . . . .	30
4.7 The Wang-Landau applied to the MPD-CT model . . . . .	30
<b>5 Results</b>	<b>33</b>
5.1 Cross-checks . . . . .	33
5.2 Grand canonical and canonical phase diagram in SC-LQCD . . . . .	36
<b>6 Discussion and Outlook</b>	<b>45</b>
<b>A One-link integral for <math>N_f = 1</math></b>	<b>47</b>
<b>B Analytic high Temperature Cross-check</b>	<b>51</b>

x

<b>C Cross-check with exact data</b>	<b>53</b>
<b>Bibliography</b>	<b>57</b>

# Motivation

In QCD details of the phase structure like the exact position of phase transitions in the grand canonical  $T-\mu$  and the canonical  $T-n$  diagram (see Fig. 1) are only conjectured, and have yet to be found. In this context lattice field theory was established but still finite density QCD is heavily impeded by the sign problem which relates to the fact that Boltzmann factors in the partition functions are not strictly positive. However, if we consider the strong coupling limit in lattice theory, the sign problem is softened by virtue of the exact integration over the gauge fields occurring in the partition function (see Sec. 3). If we further take the continuous time limit, baryons become static. Hence, we can think of an algorithm which samples the density of states  $g(B, T)$  through the underlying canonical distribution.

In this thesis we will calculate the canonical density of states  $g(B, T)$  using a combination of the continuous time worm algorithm [1] and the Wang-Landau method [2]. Notable is that in order to get the whole set  $\{g(B, T)\}_B$ , we require one single simulation. Having the density of states we can then detect the double peak structure of the grand canonical probability density  $p(\mu_B, T, B) = g(B, T)e^{\mu_B B/T} / \mathcal{Z}(\mu_B, T)$  at the first order transition line  $\mu_c(T)$  with high precision (see chapter 5). Doing so for various temperatures and extrapolating the results for different lattice volumes into the thermodynamic limit  $V \rightarrow \infty$ , we can determine the phase boundary of the co-existence region in the  $T-n_B$  plane for continuous time SC-LQCD.

The thesis is structured as follows: In chapter 1 we provide a short overview to QCD. Chapter 2 introduces the theoretical approach to lattice QCD and in chapter 3 the dual representation emerging in the strong coupling limit of lattice QCD is treated. The Wang-Landau and other methods used are established in chapter 4. The results of our approach can be found in chapter 5 and are discussed in chapter 6.

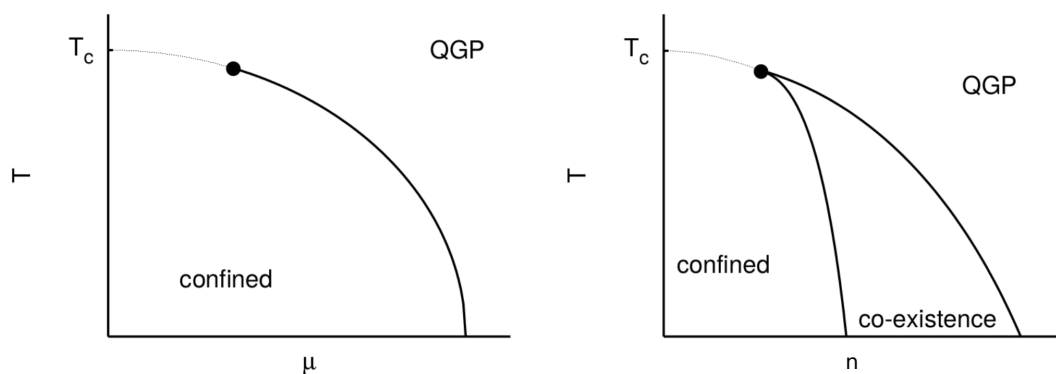


FIGURE 1: Schematic sketch of the conjectured QCD phase diagram in the grand canonical ( $T-\mu$  space) and canonical formalism ( $T-n$  space) [3].



## Chapter 1

# Introduction to Quantum Chromodynamics

The development of modern physics during the last century resulted in a successful combination of 3 of the 4 fundamental forces in the well established *standard model of particle physics* (SM). It combines electromagnetic, weak and strong interactions in one theory of which the strong interaction is of main interest in this thesis. The framework that describes strong interactions is known as *quantum chromodynamics*(QCD) which essentially is a non-trivial gauge theory. The fermions that feel the strong interaction, referred to as *quarks*, are massive, color-charged with spin- $\frac{1}{2}$  and come in several flavors called up, down, strange, charm, bottom, and top. The strong force arises from the exchange of color-charged spin-1 gauge bosons, the so called *gluons*. Of interest is that the non-Abelian nature of QCD exhibits unique phenomena like *asymptotic freedom* and *confinement*. The former implies that the coupling  $g_s$  decreases when approaching small interaction distances( $\ll 1$  fm) leading to a free field theory [4] and the latter states that only color-singlet states exists in the low energy regime which is assumed to be the case in nature. In other words, quarks are either deconfined in a quark gluon plasma in the large temperature region or confined in hadrons in the low temperature region. Alongside to confinement of quarks, we can observe the breaking of the chiral symmetry at low temperatures resulting from non-zero masses of the quarks. Lattice simulations suggest that the phase transition of both confinement to deconfinement and broken chiral symmetry to chiral restoration may coincide at the same temperature  $T_c$ , but their connection is yet unclear [5]. In order to perform calculations in quantum field theory, perturbative approaches, which rely on expanding physical quantities in terms of the coupling, are preferred. However, in QCD these methods fail at relevant distances( $\approx 1$  fm) and non-perturbative (numerical) methods have to be used.

### 1.1 Fermions in QCD

In QCD quarks come with an additional triplet quantum number called color. The reason to include the color index arose from ambiguities in bound states consisting of three quarks of the same kind(the baryons  $\Delta^{++}$ ,  $\Delta^-$  and  $\Omega^-$  consist of  $uuu$ ,  $qqq$  and  $sss$ ) seemingly violating the Pauli principle. The combination of the triplet quantum number with the Yang Mills theory led to QCD, where the corresponding color transformations are represented by elements of the SU(3) “color” group. The fermionic QCD action  $S_F[\psi, \bar{\psi}, A]$  is a bilinear functional in the quark fields  $\psi$  and  $\bar{\psi}$  given by

$$S_F[\psi, \bar{\psi}, A] = \sum_{f=1}^{N_f} \int d^4x \psi_c^{(f)} \left( \gamma_\mu (\partial_\mu \delta_{cd} + iA_{\mu,cd}) + m^{(f)} \delta_{cd} \right) \bar{\psi}_d^{(f)} \quad , \quad (1.1)$$

where  $\gamma_\mu$  with Dirac indices  $\mu = 0, 1, 2, 3$  are the  $4 \times 4$  gamma matrices in Dirac space which fulfill the relation

$$\{\gamma_\mu, \gamma_\nu\} = 2g_{\mu\nu} \mathbb{1}$$

with respect to the Minkowski metric  $g_{\mu\nu} = \text{diag}(-1, 1, 1, 1)$ .  $A_\mu$  is the gluonic field representing a non-Abelian gauge field (see Sec. 1.2) carrying two color indices. Note that the partial derivative  $\partial_\mu$  and the gauge field  $A_\mu$  are contracted by the gamma matrices  $\gamma_\mu$  with respect to  $\mu$ .

## 1.2 Gauge symmetry

In quantum field theory local gauge invariance is a substantial and powerful principle for all fundamental interactions. One of the hints to gauge invariance was the conclusion in quantum mechanics that the phase of the wave function could be chosen arbitrarily at all space-time points,

$$\psi \rightarrow \psi e^{i\phi(x)} \quad .$$

This led to a re-definition of the momentum operator in terms of *covariant* derivatives,

$$i\partial_\mu \rightarrow i\mathcal{D}_\mu = i\partial_\mu + gA_\mu$$

in order to compensate the non-vanishing derivative of  $\phi(x)$  using the redundant degrees of freedom of the gauge field  $A_\mu$ . Thus, the gauge fields themselves have to transform as

$$A_\mu \rightarrow A_\mu + \frac{i}{g} \partial_\mu \phi \quad . \quad (1.2)$$

We now introduce the color index as a new quantum number to the massive field  $\psi_i(x)$ ,  $i = 1, \dots, N_c$ . In QCD we require invariance of the actions under local color rotations of the quark fields i.e. we require invariance under the following transformations

$$\psi_i \rightarrow \Omega_{ij} \psi_j \quad \wedge \quad \bar{\psi}_i \rightarrow \bar{\psi}_j \Omega_{ji} \quad , \quad \Omega \in SU(N_c) \quad ,$$

where  $SU(N_c)$  is the *special unitary group*. Under this non-Abelian group the gauge fields  $A_\mu$  have to transform as follows

$$A_\mu \rightarrow \Omega A_\mu \Omega^{-1} - \frac{2i}{g} (\partial_\mu \Omega) \Omega^{-1} \quad .$$

Note, that we require for the gauge fields to be hermitian and traceless matrices of the form  $A_\mu = A_\mu^a T^a$ , where  $T^a$  are the generators of the corresponding group  $SU(N_c)$ .

## Chapter 2

# Lattice Quantum Chromodynamics

In this chapter a discretization of space-time will be employed in order to perform ultra-violet regularization which leads to a lattice formulation of quantum chromodynamics. In the framework of lattice quantum chromodynamic (LQCD) the path integral formalism, introduced in the first section, becomes a basic tool for statistical analysis of its thermodynamic quantities.

### 2.1 The path integral formalism

In quantum field theory the transition probability in terms of a path integral for a scalar field  $\phi(x)$ , initially being in the initial state  $|\phi, x_i\rangle$ , attaining the final state  $|\phi, x_f\rangle$  is given by [6]

$$\langle \phi, x_f | \phi, x_i \rangle = \int_{x_i}^{x_f} \mathcal{D}[\phi(x)] e^{-S_E[\phi(x)]} \quad , \quad (2.1)$$

where  $x = (\tau, \mathbf{x})$  is the Euclidean space-time position. Note, that the Euclidean time is related to the Minkowski time by the so called Wick rotation  $t = -i\tau$ ,  $\tau \in \mathbb{R}$ .<sup>1</sup> The measure is given by

$$\mathcal{D}[\phi] = \lim_{N \rightarrow \infty} \left( \frac{m}{2\pi i \epsilon} \right)^{N/2} \prod_{i=2}^N d\phi(x_i)$$

with the cut-off  $\epsilon$  of the time interval  $(\tau_i, \tau_f)$ . The Euclidean action is given by

$$S_E[\phi(x)] = \int_{\tau_{initial}}^{\tau_{final}} d\tau L_E[\phi(x)] \quad .$$

If we choose periodic boundary conditions in space position  $\mathbf{x}_i = \mathbf{x}_f$ , the transition probability Eq. (2.1) equals the partition function of statistical physics:

$$\mathcal{Z}(T) = \text{tr}[e^{-T\hat{H}}] = \int d\phi \langle \phi | e^{-T\hat{H}} | \phi \rangle = \int \mathcal{D}[\phi] e^{-S_E[\phi]} \quad ,$$

where we have dropped the explicit dependence of  $x$  for simplicity. For the expectation value of some operator  $\hat{O}$  we then obtain

$$\langle \hat{O} \rangle_T = \frac{\text{tr}[\hat{O} e^{-T\hat{H}}]}{\text{tr}[e^{-T\hat{H}}]} = \frac{1}{\mathcal{Z}(T)} \int \mathcal{D}[\phi] \mathcal{O}[\phi] e^{-S_E[\phi]} \quad . \quad (2.2)$$

<sup>1</sup>The metric  $g_{\mu\nu} = \text{diag}(-1, 1, 1, 1)$  hence becomes  $\delta_{\mu\nu} = \text{diag}(1, 1, 1, 1)$ .

Hence, on the right-hand side the operator-valued expression is replaced with a functional expression by using the path integral formalism. The exponential in Eq. (2.2) can be identified as Boltzmann weight. In the context of lattice field theory the infinite dimensional integration of the path integral (2.1) becomes finite (see Sec. 2.2) and statistical methods can be applied.

## 2.2 Discretization of fermions

The momentum cut-off in the lattice formulation of the quantum field theory serves as regularization in order to remove divergencies in the ultra-violet sector.

To do so the continuous space-time is discretized restricting the fields to a 3+1 dimensional lattice

$$\Lambda = \{n = (n_0, n_1, n_2, n_3) | n_0 = 0, \dots, N_\tau; n_1, n_2, n_3 = 0, \dots, N_\sigma\} \quad ,$$

where  $N_\tau$  and  $N_\sigma$  is the temporal extent and the spatial extent, respectively. The lattice is equipped with the spacing  $a_\tau$  and  $a_\sigma$ . For the present we set  $a = a_\tau = a_\sigma$ , and hence the space-time position is  $x = an$ .

In the following, we want to find a discrete version of the fermionic action and therefore we first take a look at the action for free fermions  $S_F^0$  in continuous space-time which is <sup>2</sup>

$$S_F^0[\psi, \bar{\psi}] = \int d^4x \bar{\psi}(x) (\gamma_\mu \partial_\mu + m) \psi(x) \quad . \quad (2.3)$$

On the lattice the fields are now restricted on the sites  $n$  and we have

$$\psi(n), \bar{\psi}(n), \quad n \in \Lambda \quad .$$

The mass term simply becomes

$$m \bar{\psi}(x) \psi(x) \rightarrow m \bar{\psi}(n) \psi(n)$$

and for the partial derivative of the kinetic term we use the symmetric form of the differential

$$\partial_\mu \psi(x) \rightarrow \frac{\psi(n + \hat{\mu}) - \psi(n - \hat{\mu})}{2a} \quad ,$$

where  $\hat{\mu}$  implies a unit into space-time direction on the lattice. The integral is replaced with a finite sum like

$$\int d^4x \rightarrow a^4 \sum_n \quad .$$

In order to get a dimensionless expression we absorb the factor  $\sqrt{a^3}$  into the fields by defining  $\sqrt{a^3} \psi \rightarrow \psi$  and  $\sqrt{a^3} \bar{\psi} \rightarrow \bar{\psi}$ . Thus, a naive lattice version of the free action can be of the form

$$S_F^0[\psi, \bar{\psi}] = \sum_{n \in \Lambda} \bar{\psi}(n) \left( \sum_{\nu=0}^3 \gamma_\nu \frac{\psi(n + \hat{\nu}) - \psi(n - \hat{\nu})}{2} + am \psi(n) \right) \quad . \quad (2.4)$$

If we now want to include invariance under local rotations of color indices, we have to introduce a so-called link variable  $U_\mu$  which is the lattice analogon to the gauge field  $A_\mu$ . They are related by the path ordered transport equation and on the lattice

<sup>2</sup>Color and flavour components are implicit in the vectorial notation.

the relation becomes (chapter 2 in [7])

$$U_\mu(n) = e^{iaA_\mu(n)} . \quad (2.5)$$

We require invariance under the following local transformations

$$\psi(n) \rightarrow \psi(n)' = \Omega(n)\psi(n) \quad \wedge \quad \bar{\psi}(n) \rightarrow \bar{\psi}(n)' = \bar{\psi}(n)\Omega(n)^\dagger .$$

The field  $U_\mu(n)$  has the transformation property

$$U_\mu(n) \rightarrow U_\mu(n)' = \Omega(n)U_\mu(n)\Omega(n+\hat{\mu})^\dagger .$$

Introducing the lattice gauge field  $U_\mu$  in the kinetic term, we obtain the following invariant expression:

$$\begin{aligned} \bar{\psi}(n)'U_\mu(n)'\psi(n+\hat{\mu})' &= \bar{\psi}(n)\Omega(n)^\dagger\Omega(n)U_\mu(n)\Omega(n+\hat{\mu})^\dagger\Omega(n+\hat{\mu})\psi(n+\hat{\mu}) \\ &= \bar{\psi}(n)U_\mu(n)\psi(n+\hat{\mu}) . \end{aligned}$$

The naive lattice action for free fermions then generalizes to <sup>3</sup>

$$S_F[\psi, \bar{\psi}, U] = \sum_{n \in \Lambda} \bar{\psi}(n) \left( \sum_{\nu=0}^3 \gamma_\nu \frac{U_\nu(n)\psi(n+\hat{\nu}) - U_{-\nu}(n)\psi(n-\hat{\nu})}{2} + am\psi(n) \right) , \quad (2.6)$$

which reproduces the continuous action Eq. (1.1) by taking the continuum limit  $a \rightarrow 0$ .

Though, it turns out that this lattice version of the fermionic action comprises additional poles in the propagator. Hence, it describes the wrong number of flavors. To make this apparent we consider the free fermion case  $U = \mathbb{1}$  and rewrite (2.6) into an explicit quadratic form

$$S_F[\psi, \bar{\psi}, U] = \sum_{n, m \in \Lambda} \bar{\psi}(n) D(n|m) \psi(m) , \quad (2.7)$$

where the Dirac operator  $D(n|m)$  is given by

$$D(n|m) = \sum_{\mu=0}^3 \gamma_\mu \frac{\delta_{n+\hat{\mu}, m} - \delta_{n-\hat{\mu}, m}}{2} + am\delta_{n, m} .$$

Wick's theorem tells us that the propagator is given by the inverse of the Dirac operator  $D(n|m)^{-1}$ . The calculation of the inverse of  $D(n|m)$  is done in [7] by proceeding as follows. First we change into Fourier space  $\tilde{D}(p|q)$  and then take advantage of the diagonal form with respect to the variables  $p, q$  to get the inverse  $\tilde{D}(p|q)^{-1}$ . The propagator  $D(n|m)^{-1}$  is obtained by transforming back to the original space. The propagator in momentum space is given by

$$\tilde{D}(p)^{-1} = \frac{am\mathbb{1} - i\sum_{\mu=0}^3 \gamma_\mu \sin(p_\mu a)}{(am)^2 + \sum_{\mu=0}^3 \sin(p_\mu a)^2} . \quad (2.8)$$

The momenta are restricted to the first Brillouin zone  $p_\mu \in (-\frac{\pi}{a}, \frac{\pi}{a}]$  and we will have poles if either  $p_\mu = 0$  or  $p_\mu = \frac{\pi}{a}$  for every  $\mu = 0, 1, 2, 3$ . This results in a total of 16

<sup>3</sup>The orientations in directions  $\hat{\mu}$  and  $-\hat{\mu}$  of the link variable are related via  $U_\mu(n)^\dagger = U_{-\mu}(n-\hat{\mu})$ .

poles. So we have 15 additional poles which are referred to as doublers [7].

### 2.3 Staggered fermions

The idea of staggered fermions is to reduce the number of doublers as present in the fermion action Eq. (2.6) from 16 to 4. This is done by a space-time dependent transformation of the fields  $\psi(x)$  and  $\bar{\psi}(x)$ .<sup>4</sup>

The fields are transformed as follows:

$$\psi(x) = \gamma_0^{n_0} \gamma_1^{n_1} \gamma_2^{n_2} \gamma_3^{n_3} \psi(x)' = \Gamma(x) \psi(x)'$$

and

$$\bar{\psi}(x) = \bar{\psi}(x)' \gamma_3^{n_3} \gamma_2^{n_2} \gamma_1^{n_1} \gamma_0^{n_0} = \bar{\psi}(x)' \Gamma(x)^\dagger .$$

Inserting this into Eq. (2.6) we will observe that this transformation leaves the mass term unchanged because the  $\gamma$ -matrices fulfill  $\gamma_\mu^2 = \mathbb{1}$ , and hence  $\Gamma(x)^\dagger \Gamma(x) = \mathbb{1}$ . For  $\mu \neq \nu$  it holds  $\gamma_\mu \gamma_\nu = -\gamma_\nu \gamma_\mu$ . The kinetic term then transforms as

$$\begin{aligned} \bar{\psi}(x) \gamma_\mu \psi(x) &= \bar{\psi}(x)' \Gamma(x)^\dagger \gamma_\mu \Gamma(x) \psi(x)' = (-1)^{\sum_{i=0}^{\mu-1} n_i} \bar{\psi}(x)' \psi(x)' \\ &= \eta_\mu(x) \bar{\psi}(x)' \psi(x)' , \end{aligned}$$

where the  $\gamma$ -matrices are absorbed into a space-time dependent sign function, the so-called *staggered phase*  $\eta_\mu(x) = (-1)^{\sum_{i=0}^{\mu-1} n_i}$ . The fermionic action Eq. (2.6) then becomes

$$S_F[\psi', \bar{\psi}', U] = \sum_x \bar{\psi}(x)' \left( \sum_{\nu=0}^3 \eta_\nu(x) \frac{U_\nu(x) \psi(x + \hat{\nu})' - U_{-\nu}(x) \psi(x - \hat{\nu})'}{2} + am \psi(x)' \right) ,$$

and therefore is diagonal in Dirac space which means we have the same equation for every spinor component. Subsequently, we can reduce four equations to one equation by defining

$$S_F[\chi, \bar{\chi}, U] = \sum_x \bar{\chi}(x) \left( \sum_{\nu=0}^3 \eta_\nu(x) \frac{U_\nu(x) \chi(x + \hat{\nu}) - U_{-\nu}(x) \chi(x - \hat{\nu})}{2} + am \chi(x) \right) , \quad (2.9)$$

where  $\chi(x)$  and  $\bar{\chi}(x)$  are one dimensional spinor fields with only color indices. In other words we put only one out of 4 spinor components on each lattice site which divides the number of doubler by 4. For further details see [7].

### 2.4 Temperature in lattice QCD

In lattice QCD, we want to analyse thermodynamic properties for temperatures other than  $T = 0$ . Hence, the temporal extent in the Euclidean action have to be restricted by

$$S_E[\psi, \bar{\psi}] = \int_0^\beta d\tau \int_{\mathbb{R}^3} d^3\mathbf{x} L[\psi, \bar{\psi}] .$$

For the lattice  $\Lambda$  defined in section (2.2) this means we have to fix the temporal extent at

$$aN_\tau = \frac{1}{T} = \beta . \quad (2.10)$$

<sup>4</sup>The space-time position  $x$  is related to the lattice site  $n \in \Lambda$  by:  $x = an$  (see section 2.2).

The Continuum limit is now taken by letting  $a \rightarrow 0$  keeping  $aN_\tau = \beta$  and  $a|\Lambda_\sigma|$  fixed, where  $|\Lambda_\sigma|$  is the spatial size.

In order to get results for various temperatures with fixed spacing  $a$  we have to use different temporal extents  $N_\tau$ . Therefore, we are restricted to discrete set of temperatures. In addition, there are only temperatures available not higher than  $aT = 1/N_\tau = 1/2$  because for fermions we have to choose anti-periodic boundary conditions in temporal direction which restricts its minimal size to  $N_\tau = 2$ . Since chiral restoration is given for temperatures at about  $aT \simeq 1.5$ , we could then not study physics of interest.

To fix this problem we apply a slight modification to the fermionic action Eq. (2.6) of the form

$$S_F[\psi, \bar{\psi}, U] = \sum_x \bar{\psi}(x) \left( \sum_{\nu=1}^3 \gamma_\nu \frac{U_\nu(x)\psi(x + \hat{\nu}) - U_{-\nu}(x)\psi(x - \hat{\nu})}{2} + \gamma \gamma_0 \frac{U_\delta(x)\psi(x + \hat{0}) - U_{-\delta}(x)\psi(x - \hat{0})}{2} + am \psi(x) \right).$$

where  $\gamma$  is the *bare-anisotropy parameter*. This modification implies that, if  $\gamma \neq 1$ , the action is no longer symmetric with respect to exchanges of the temporal axis with a spatial one. In particular, the correlation length  $\xi_\tau$  in temporal direction will differ from the spatial correlation length  $\xi_\sigma$ . At this point we can say that the lattice has become anisotropic and the temporal spacing  $a_\tau$  varies with  $\gamma$ . We can argue that in physical units the correlation length for different directions should equal each other and the following holds

$$\xi_\tau a_\tau = \xi_\sigma a_\sigma$$

where  $a_\sigma$  is the lattice spacing in spatial direction. Defining the  $\gamma$ -dependent *anisotropy parameter*  $\xi = a_\sigma/a_\tau$  and using Eq. (2.10) we can write

$$a_\sigma T = \frac{\xi(\gamma)}{N_\tau} \quad (2.11)$$

which allows us to change the temperature continuously at fixed  $a_\sigma$  [8].

## 2.5 The chemical potential in lattice QCD

In order to include non-vanishing particle densities a chemical potential  $\mu$  have to be introduced on the lattice. In statistical physics we have for a quantum mechanical system the grand canonical partition function

$$\mathcal{Z}(T, \mu) = \text{tr}[e^{-(\hat{H} - \mu \hat{N})/T}] ,$$

where  $\hat{N}$  is the particle number operator. The term  $\mu \hat{N}/T$  gives rise to an additional term in the lattice version of the fermionic action Eq. (2.6) which would be of the form

$$\sum_x \mu \bar{\psi}(x) \gamma_0 \psi(x) ,$$

where we use that the space integral over the zero component of the Noether current  $j_\mu = \bar{\psi}(x) \gamma_0 \psi(x)$  is the particle number  $N = \sum_x \bar{\psi}(x) \gamma_0 \psi(x)$ . However, this naive approach would run into problems in the continuum limit  $a \rightarrow 0$  since the energy density  $\epsilon$  becomes proportional to  $(\mu/a)^2$  instead of being  $\epsilon \propto \mu^4$  [9]. A correct

implementation would be the modification of the temporal link variable by multiplying it with the additional factor  $e^{a\mu}$ . The fermionic action Eq. (2.6) then becomes

$$S_F[\psi, \bar{\psi}, U] = \sum_x \bar{\psi}(x) \left( \sum_{\nu=1}^3 \gamma_\nu \frac{U_\nu(x)\psi(x + \hat{\nu}) - U_{-\nu}(x)\psi(x - \hat{\nu})}{2} + \gamma_0 \frac{e^{a\mu} U_0(x)\psi(x + \hat{0}) - e^{-a\mu} U_{-\hat{0}}(x)\psi(x - \hat{0})}{2} + am \psi(x) \right). \quad (2.12)$$

For the interpretation we take a look at the continuous Lagrangian with chemical potential  $\mu$  which is given by

$$\begin{aligned} L[\psi, \bar{\psi}] &= \bar{\psi}(x) \left( \gamma_\mu (\partial_\mu + igA_\mu(x)) + \gamma_0 \mu + m \right) \psi(x) \\ &= \bar{\psi}(x) \left( \gamma_\mu (\partial_\mu + igA_\mu(x) + \mu\delta_{\mu,0}) + m \right) \psi(x). \end{aligned}$$

Hence, the chemical potential could be understood as imaginary part of the (scalar) gauge potential. So we have to introduce the gauge fields  $U_\mu(x) = e^{iaA_\mu(x)}$  with the new gauge potential  $A_\mu \rightarrow A_\mu - i\mu\delta_{\mu,0}$ . Thus, we have  $U_0(x) \rightarrow e^{a\mu} U_0(x)$ .

## Chapter 3

# Strong coupling lattice QCD at finite baryon-number density

To study finite baryon densities on the lattice either a fixed non-zero baryon chemical potential  $\mu_B$  or a fixed non-zero baryon number  $B$  has to be introduced in the partition function leading to a grand canonical and canonical formulation, respectively. Both formulations, the grand canonical with fixed  $\mu_B$  and the canonical with fixed  $B$ , suffer from negative Boltzmann factors occurring in the partition function which is referred to as sign problem. In strong coupling lattice QCD (SC-LQCD) with staggered fermions and gauge fields from  $SU(N_c)$ , Rossi and Wolff [10] introduced a new representation of the partition function in which this problem softens. The idea is that by taking the limit  $\beta \rightarrow 0$ , the Wilson plaquette term, describing the gluonic part (see Chapter 2 in [7]), is suppressed and we can integrate out the gauge and subsequently the fermion fields explicitly. It turns out that the partition function becomes equal to a system of monomers, dimers and polymers (see Sec. 3.1). By additionally taking the continuous time limit, the baryons become static and the sign problem is completely absent (see Sec. 3.3).

### 3.1 The monomer, dimer and polymer model

In the strong coupling limit ( $\beta \rightarrow 0$ ) the partition function with Grassmann valued staggered fermion fields,  $SU(N_c)$  gauge fields and the quark chemical potential  $\mu_q$  is given by

$$\mathcal{Z}(\mu_q, T, m_q) = \int \mathcal{D}[\chi, \bar{\chi}] \mathcal{D}[U] e^{S_F[\chi, \bar{\chi}, U]} \quad , \quad (3.1)$$

where the staggered action for one flavor is (for a short derivation see section 2.3)<sup>1</sup>

$$S_F[\chi, \bar{\chi}, U] = \sum_x \left\{ \sum_{\mu=0}^3 \eta_\mu(x) \left( \bar{\chi}(x) U_{\hat{\mu}}(x) \chi(x + \hat{\mu}) - \bar{\chi}(x + \hat{\mu}) U_{\hat{\mu}}^\dagger(x) \chi(x) \right) + 2am_q \bar{\chi}(x) \chi(x) \right\} \quad (3.2)$$

We provide the system, described by Eq. (3.1), with periodic boundary conditions with respect to spatial directions and anti-periodic boundary conditions in temporal direction. Note, that the temporal link variable is prescribed with  $U_{\pm\hat{0}}(x) \rightarrow \gamma e^{\pm a\tau\mu_q} U_{\pm\hat{0}}(x)$ , where  $\gamma$  is the *anisotropic-coupling parameter* from section 2.4 and the exponential  $e^{\pm a\tau\mu_q}$  of the chemical potential is derived in section 2.5. To integrate over the gauge fields  $U_{\mu_q}$  the partition function Eq. (3.1) is rewritten into the more

<sup>1</sup>The fields in the action Eq. (2.9) are rescaled by the factor  $\chi \rightarrow i\sqrt{2}\chi$  and  $\bar{\chi} \rightarrow i\sqrt{2}\bar{\chi}$  to cancel the sign in the exponential of the partition function and the  $1/2$  factor appearing in the action. We also rewrite  $\sum_x \bar{\chi}(x) U_\mu(x)^\dagger \chi(x - \hat{\mu})$  to the equivalent form  $\sum_x \bar{\chi}(x + \hat{\mu}) U_\mu(x)^\dagger \chi(x)$  w.r.t. the boundary conditions.

advantageous form:

$$\begin{aligned} \mathcal{Z} &= \int \prod_x d\chi(x) d\bar{\chi}(x) e^{2am_q \bar{\chi}(x)\chi(x)} \prod_\mu dU_{\hat{\mu}}(x) e^{\eta_\mu(x) (\bar{\chi}(x)U_{\hat{\mu}}(x)\chi(x+\hat{\mu}) - \bar{\chi}(x+\hat{\mu})U_{\hat{\mu}}^\dagger(x)\chi(x))} \\ &\equiv \int \prod_x d\chi(x) d\bar{\chi}(x) e^{2am_q \bar{\chi}(x)\chi(x)} \prod_\mu z(x, \mu) \quad . \end{aligned} \quad (3.3)$$

Performing the integration over one single link  $U_\mu$  on site  $x$  (see appendix A) we get

$$\begin{aligned} z(x, \mu) &= \sum_{k=0}^{N_c} \left\{ \frac{(N_c - k)!}{N_c! k!} \left( (\eta_{\hat{\mu}}(x) \gamma^{\delta_{0,\mu}})^2 \bar{\chi}(x)\chi(x)\bar{\chi}(y)\chi(y) \right)^k \right\} \\ &\quad + \frac{1}{N_c!} \left( (\rho(x, y) \bar{\chi}(x)\chi(y))^{N_c} + (-1)^{N_c} (\rho(y, x) \bar{\chi}(y)\chi(x))^{N_c} \right) \\ &= \sum_{k=0}^{N_c} \left\{ \frac{(N_c - k)!}{N_c! k!} \left( (\eta_{\hat{\mu}}(x) \gamma^{\delta_{0,\mu}})^2 M(x)M(y) \right)^k \right\} \\ &\quad + (\rho(x, y))^{N_c} \bar{B}(x)B(y) + (-1)^{N_c} (\rho(y, x))^{N_c} \bar{B}(y)B(x) \quad , \end{aligned} \quad (3.4)$$

where  $y$  is related to  $x$  by  $y = x + \hat{\mu}$  and  $k \equiv k_{\hat{\mu}}(x) \in \{0, \dots, N_c\}$  is referred to as *mesonic link variable* (occupation number). Additionally, we have

$$\rho(x, y) = \eta_{\hat{\mu}}(x) \begin{cases} \gamma \exp(\pm a_\tau \mu_q), & (y - x) = \pm 1 \\ 1 & \text{else} \end{cases} \quad .$$

The fermionic fields  $\chi(x)$  and  $\bar{\chi}(x)$  are absorbed into mesonic fields  $M(x)$  and (anti)baryonic fields  $B(x)$  and  $\bar{B}(x)$  by defining

$$\begin{aligned} M(x) &\equiv \bar{\chi}(x)\chi(x) \quad , \\ B(x) &\equiv \frac{1}{N_c!} \epsilon_{i_1, \dots, i_{N_c}} \chi_{i_1}(x) \cdots \chi_{i_{N_c}}(x) \quad \text{and} \quad \bar{B}(x) \equiv \frac{1}{N_c!} \epsilon_{i_1, \dots, i_{N_c}} \bar{\chi}_{i_{N_c}}(x) \cdots \bar{\chi}_{i_1}(x) \quad . \end{aligned}$$

Inserting Eq. (3.4) into the full integral Eq. (3.3) and taking the product over  $x$  and  $\mu$ , possible contributions in the product in Eq. (3.3) come from integrals of the type

$$\begin{aligned} &\int d\chi(x) d\bar{\chi}(x) e^{2am_q \bar{\chi}(x)\chi(x)} (\bar{\chi}(x)\chi(x))^{n_D(x)} \\ &= \sum_{\ell=0}^{\infty} \frac{1}{\ell!} \int d\bar{\chi}(x) (2am_q \bar{\chi}(x)\chi(x))^\ell (\bar{\chi}(x)\chi(x))^{n_D(x)} \\ &= \frac{N_c!}{(N_c - n_D(x))!} (2am_q)^{N_c - n_D(x)} = \frac{N_c!}{(n_M(x))!} (2am_q)^{n_M(x)} \quad . \end{aligned} \quad (3.5)$$

For the last equation we used the integral relation of Grassmann variables  $\int d\bar{\xi} d\xi \bar{\xi} \xi = 1$  and  $n_D(x) \in \{0, \dots, N_c\}$  is the site dependent dimer number which tells us how much mesonic links (dimers)  $M(x)M(y)$  are touching the site  $x$ , i.e.  $n_D(x) = \sum_{\hat{\mu}=\pm\hat{0}, \dots, \pm\hat{3}} k_{\hat{\mu}}(x)$ . We replaced  $N_c - n_D(x)$  with  $n_M(x)$  which we will refer to as the *monomer number*. Hence, contributions on site  $x$  come from combinations of mesonic links and additional fields coming from the mass term (see Eq. 3.5), called monomers, where both are related via the constraint

$$n_M(x) \equiv N_c - n_D(x) \quad . \quad (3.6)$$

Baryonic fields have contributions in the product term, if there is a product of an incoming baryonic link  $\bar{B}(y)B(x)$  with an outgoing baryonic link  $\bar{B}(x)B(z)$  for  $y = x + \hat{\mu} \neq x + \hat{\nu} = z$  because baryonic fields already contain all necessary Grassmann variables  $\chi_i(x), i \in \{1, \dots, N_c\}$ . Thus, we can derive an additional constraint

$$\sum_{\hat{\rho}=\pm\hat{0},\dots,\pm\hat{3}} b_{\hat{\rho}} = 0 \quad , \quad (3.7)$$

where the *baryonic link variable*  $b_{\hat{\rho}} \in \{-1, 0, 1\}$  is  $b_{\hat{\rho}} = -1$  for the incoming baryonic link and  $b_{\hat{\nu}} = 1$  for the outgoing one.

Possible configurations (see Fig. 3.1) consist of sites connected by oriented self-

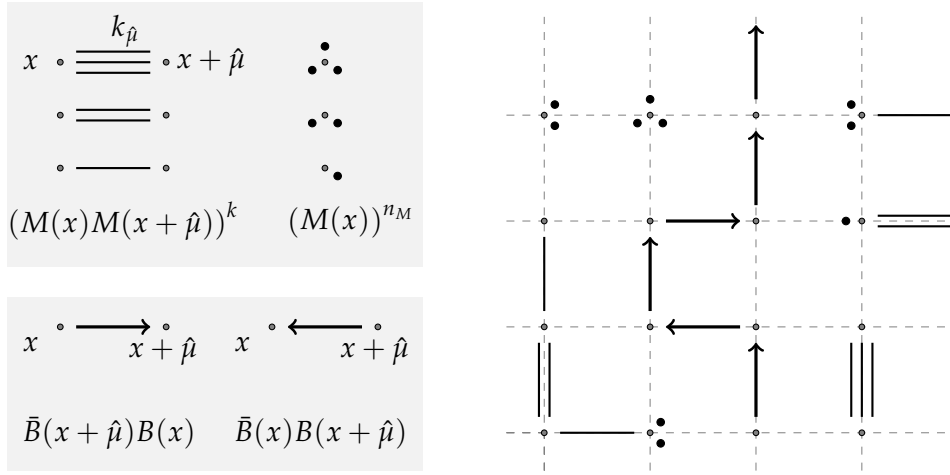


FIGURE 3.1: The right figure outlines the graphical notation of monomers and mesonic(top) and baryonic(bottom) link variables for  $SU(3)$ , where the left figure shows a illustrative configuration in 2-dimensional MDP system. Grey dots denotes lattice sites.

avoiding baryonic loops satisfying the constraint (3.7). Combinations of monomers and dimers, fulfilling (3.6), make up the remaining sites.

To summarize, integrating out the fields  $\chi, \bar{\chi}$  and  $U$  leads to a new representation of the partition function Eq. (3.1) through a new variable set  $\{n_M, k, \ell\}$  following the (local) color constraint

$$N_c = n_M(x) + \sum_{\hat{\rho}=\pm\hat{0},\dots,\pm\hat{d}} \left( k_{\hat{\rho}}(x) + \frac{N_c}{2} |b_{\hat{\rho}}(x)| \right) \quad (3.8)$$

which combines both constraints (3.6) and (3.7), where

- $n_M(x) \in \{0, \dots, N_c\}$  denotes the monomer number and results from mesonic fields  $M(x)^{n_M}$  which are generated by the mass term  $e^{2am\bar{\chi}\chi}$ .
- the mesonic link occupation number  $k_{\hat{\rho}} \in \{0, \dots, N_c\}$  arising from non-oriented mesonic hoppings  $(M(x)M(x + \hat{\mu}))^k$ .
- And baryon loops  $\ell$  coming from oriented baryon hoppings  $\bar{B}(x)B(x + \hat{\mu})$  forming self-avoiding oriented loops. We can assign to each site  $x \in \Lambda_B$  a baryon link variable  $b_{\hat{\rho}/\hat{\nu}}(x) = \pm 1$ , where  $\hat{\mu}$  is the outgoing direction and  $\hat{\rho}$  the incoming one.

The full partition function in the new representation becomes

$$\mathcal{Z} = \sum_{\{n_M, k, \ell\}} \prod_{x \in \Lambda_M, \hat{\mu}} \frac{(N_c - k_{\hat{\mu}}(x))!}{N_c! k_{\hat{\mu}}(x)!} \gamma^{2k_{\hat{\mu}}(x)\delta_{\hat{0}, \hat{\mu}}} \prod_x \frac{N_c!}{n_M(x)!} (2am_q)^{n_M(x)} \prod_{\ell} \omega(\ell) \quad (3.9)$$

, where the first term is the contribution of the mesonic part with the set  $\Lambda_M$  containing all mesonic sites, the second is the contribution of the monomers and the last is the baryonic contribution and is given by the product of

$$\omega(\ell) = \sigma(\ell) \prod_{(x, \hat{\mu}) \in \mathcal{C}_{path}(\ell)} \frac{1}{N_c!} \gamma^{N_c \delta_{\hat{\mu}, \hat{0}}} \exp(N_c N_{\tau} r_{\ell} a_{\tau} \mu_q)$$

over the loops  $\ell$ , where the sign  $\sigma(\ell)$  is

$$\sigma(\ell) = (-1)^{r_{\ell} + N_{-}(\ell) + 1} \prod_{x, \hat{\mu} \in \mathcal{C}_{path}(\ell)} \eta_{\hat{\mu}}(x) \quad . \quad (3.10)$$

The following parameters characterize the loop geometry: The winding number  $r_{\ell}$  in  $\hat{0}$ -direction, the number of links in negative directions  $N_{-}(\ell)$  and the path  $\mathcal{C}_{path}(\ell)$  containing all sites and directions  $\{x, \hat{\mu}\}$  visited by the baryonic loop.

## 3.2 The sign

For  $\mu_B = 0$  the system, given by Eq. (3.9), has strictly positive weights after performing a resummation [11]. However, for finite baryon density the sign problem is still present. Though, within the dual representation it is mildened and we can overcome it by performing sign reweighting of observables using the "average sign" given by

$$\langle \mathcal{O} \rangle \equiv \frac{\langle \sigma \mathcal{O} \rangle_{||}}{\langle \sigma \rangle_{||}} \quad , \quad \langle \sigma \rangle_{||} = \exp\left(\frac{V}{T} \Delta f\right) \quad ,$$

where  $V$  is the lattice volume and  $\Delta f \equiv f(T, \mu, m_q)$  is the difference in the free energy which reflects the severity of the sign [4].

## 3.3 The continuous time limit

In this section we will derive a continuous time version of the partition function in the dual representation. The advantage of having a continuous time formulation is that lattice artifacts, coming from the discretization, are prevented. Further, we can design algorithms which estimates critical temperatures more precisely without the necessity of extrapolations in time direction. Another benefit is that baryons become static, hence the sign problem completely disappears.

In order to vary the temporal lattice spacing continuously we introduced in section 2.4 the *bare coupling*  $\gamma$  which controls the lattice temperature by the relation

$$aT = \frac{\xi(\gamma)}{N_{\tau}} \quad ,$$

where  $\xi(\gamma)$  is the *anisotropy parameter*. Its functional dependence on  $\gamma$  is unknown but results from non-perturbative studies, done in [12], suggest that

$$\xi(\gamma) = \kappa\gamma^2 + \frac{\gamma^2}{1 + \lambda\gamma^4} \quad , \quad \kappa = 0.781 \quad ,$$

where the coefficient  $\lambda$  is given by  $\lambda = \kappa/(1 + \kappa)$  such that  $\xi(1) = 1$ . Thus, for large  $\gamma$  the temperature behaves as  $aT = \kappa\gamma^2/N_\tau$  which is a significant improvement over  $aT = \gamma^2/N_\tau$  suggested by mean field approximations.

The goal in the continuous time formulation is to remove the dependence on  $\gamma$  and  $N_\tau$  in Eq. (3.9) by taking the limits  $\gamma \rightarrow \infty$  and  $N_\tau \rightarrow \infty$  keeping  $\kappa\gamma^2/N_\tau = aT$  fixed, thus replacing them with the temperature  $aT$ .

### 3.3.1 $\gamma$ and $N_\tau$ large

We start by considering the chiral limit,  $m_q = 0$ , in which monomers are absent. Therefore, the set  $\Lambda$  decomposes into the two disjoint subsets  $\Lambda = \Lambda_M \sqcup \Lambda_B$ , where  $\Lambda_M$  contains all sites connected with dimers and  $\Lambda_B$  contains all sites connected with baryonic links. In the following, we can rewrite Eq. (3.9) by pulling out the overall factor  $\gamma^{N_c|\Lambda|}$  such that all spatial dimers and spatial baryonic links obtain a factor  $\gamma^{-2}$  and  $\gamma^{-N_c}$ , respectively. We have:

$$\begin{aligned} \mathcal{Z}(\gamma, N_\tau) &= \sum_{\{k, \ell\}} \prod_{x \in \Lambda_{M, \hat{\mu}}} \frac{(N_c - k_{\hat{\mu}}(x))!}{N_c! k_{\hat{\mu}}(x)!} \gamma^{2k_{\hat{\mu}}(x)\delta_{\hat{0}, \hat{\mu}}} \prod_{x \in \Lambda} N_c! \prod_{\ell} \omega(\ell) \quad , \quad \text{for } m_q = 0 \\ &= \sum_{\{k, \ell\}} \gamma^{(\sum_{x \in \Lambda_{M, \hat{\mu}}} 2k_{\hat{\mu}}\delta_{\hat{\mu}, \hat{0}} + \sum_{x \in \Lambda_{B, \hat{\mu}}} N_c |b_{\hat{\mu}}|\delta_{\hat{\mu}, \hat{0}})} \prod_{x \in \Lambda_{M, \hat{\mu}}} \frac{(N_c - k_{\hat{\mu}}(x))!}{N_c! k_{\hat{\mu}}(x)!} \prod_{x \in \Lambda} N_c! \prod_{\ell} \omega'(\ell) \\ &= \sum_{\{k, \ell\}} \gamma^{N_c|\Lambda| + (\sum_{x \in \Lambda_{M, \hat{\mu}}} 2k_{\hat{\mu}}\delta_{\hat{\mu}, \hat{i}} + \sum_{x \in \Lambda_{B, \hat{\mu}}} N_c |b_{\hat{\mu}}|\delta_{\hat{\mu}, \hat{i}})} \prod_{x \in \Lambda_{M, \hat{\mu}}} \frac{(N_c - k_{\hat{\mu}}(x))!}{N_c! k_{\hat{\mu}}(x)!} \prod_{x \in \Lambda} N_c! \prod_{\ell} \omega'(\ell) \\ &= \gamma^{N_c|\Lambda|} \left( \sum_{\{k, \ell\}} \prod_{x \in \Lambda_M} \left( \prod_{\hat{i}=\hat{1}}^{\hat{3}} \frac{(N_c - k_{\hat{i}})!}{k_{\hat{i}}!} \gamma^{-2k_{\hat{i}}} \right) \frac{(N_c - k_{\hat{0}})!}{k_{\hat{0}}!} \prod_{\ell \in \Lambda_B} \tilde{\omega}(\ell) \right) \quad , \end{aligned} \quad (3.11)$$

where we used that

$$\begin{aligned} N_c|\Lambda| &= \sum_{x \in \Lambda_{M, \hat{\mu}}} 2k_{\hat{\mu}} + \sum_{x \in \Lambda_{B, \hat{\mu}}} N_c |b_{\hat{\mu}}| \\ &= \left( \sum_{x \in \Lambda_{M, \hat{\mu}}} 2k_{\hat{\mu}}\delta_{\hat{\mu}, \hat{i}} + \sum_{x \in \Lambda_{B, \hat{\mu}}} N_c |b_{\hat{\mu}}|\delta_{\hat{\mu}, \hat{i}} \right) + \left( \sum_{x \in \Lambda_{M, \hat{\mu}}} 2k_{\hat{\mu}}\delta_{\hat{\mu}, \hat{0}} + \sum_{x \in \Lambda_{B, \hat{\mu}}} N_c |b_{\hat{\mu}}|\delta_{\hat{\mu}, \hat{0}} \right) \end{aligned}$$

for a system in the chiral limit. The baryonic part is first substituted by

$$\omega'(\ell) = \sigma(\ell) \prod_{(x, \hat{\mu}) \in \mathcal{C}_{path}(\ell)} \frac{1}{N_c!} \exp(N_c N_\tau r_\ell a_\tau \mu_q) \quad .$$

and lastly becomes

$$\tilde{\omega}(\ell) = \sigma(\ell) \prod_{(x, \hat{\mu}) \in \mathcal{C}_{path}(\ell)} \gamma^{-N_c \delta_{\hat{\mu}, \hat{i}}} \exp(N_c N_\tau r_\ell a_\tau \mu_q) \quad . \quad (3.12)$$

Furthermore, the factor

$$\frac{1}{N_c!^{|\Lambda|}} = \frac{1}{N_c!^{|\Lambda_M|} N_c!^{|\Lambda_B|}} .$$

coming from the mesonic- and baryonic part in Eq. (3.11) becomes the same for all weights, and hence cancels the factor  $N_c!^{|\Lambda|}$  coming from the remanent monomer part. In the subsequent calculations the overall factors in front of the partition function can be omitted since they cancel for observables due to the weighting (2.2).

Considering large  $\gamma$  and  $N_\tau$  we make the following observations:

- All spatial dimer with  $k_i(x) > 1$  are suppressed. Single spatial dimers survive since the summation over  $N_\tau$  sites is proportional to  $\mathcal{O}(\gamma^2)$ . Thus, the mesonic contribution becomes

$$\underset{\gamma \rightarrow \infty}{=} \prod_{x \in \Lambda_M} \left( \delta_{k_i,0} + \delta_{k_i,1} \frac{\gamma^{-2}}{N_c} \right) \frac{(N_c - k_\delta)!}{k_\delta!} .$$

- In temporal direction dimers can either arrange in 2-1-chains ( $= \cdot - \cdot$ ) with contributions  $(N_c - k_\delta)!/k_\delta! = 1/2, 2$  for altering  $k_\delta = 2, 1$  or 3-0-chains ( $\equiv \cdot \cdot$ ) with contributions  $(N_c - k_\delta)!/k_\delta! = 1/3, 3$ , when fixing color to  $N_c = 3$ . Hence, temporal dimer chains of any length do not change the partition function. For future notation dimer chains without any spatial dimer attached are referred to as static mesonic lines.
- In the mesonic product the only contributions come from sites  $x$  connected with single spatial dimers. These sites can be interpreted as vertices either having a T-form or a L-form with contributions  $v_T = \frac{2}{\sqrt{3}}\gamma^{-1} = \hat{v}_T\gamma^{-1}$  and  $v_L = \gamma^{-1} = \hat{v}_L\gamma^{-1}$  (see Fig. 3.2), where  $\hat{v}_T = 2/\sqrt{3}$  and  $\hat{v}_L = 1$ . The mesonic part in the vertex formulation is given by

$$\underset{\gamma \rightarrow \infty}{=} \prod_{x \in \Lambda_M} v_T^{n_T(x)} v_L^{n_L(x)} ,$$

where  $n_T(x) = 0, 1$  and  $n_L(x) = 0, 1$  is the number of vertices on site  $x \in \Lambda_M$ . Note, one spatial dimer corresponds to two vertices and the number of spatial dimers connected to a dimer chain is always even.

- The lattice becomes bipartite and spatial dimers are now oriented being emitted/absorbed from an "emission site"/"absorption site" lowering/rising the "state" of dimer chains. These states can be interpreted as quantum numbers in the Hamiltonian formulation of continuous time which has "spin" raising/lowering operators. For  $N_c = 3$ , the "spin states" for the four different static mesonic lines range within  $\{3/2, 1/2, -1/2, -3/2\}$  [13].
- The sum in  $N_\tau$  is of order  $\mathcal{O}(\gamma^2)$ . Hence, for  $N_c = 3$  spatial baryonic contributions are suppressed by  $\gamma^{-1} = \gamma^2/\gamma^3$ . Only contributions from baryonic loops in time direction remain (static baryons). Since  $N_\tau$  is even and the winding number becomes  $r_\ell = -1, 1$  for antibaryons and baryons the sign (3.10) is always positive and the sign problem is absent. Thus, we can rewrite the

baryonic contribution as follows:

$$\prod_{\ell \subset \Lambda_B} \tilde{\omega}(\ell) \stackrel{\gamma \rightarrow \infty}{=} \prod_{x \in \Lambda_B^3} e^{3r_\ell \mu_q a_\tau N_\tau} = e^{3\mu_q B a_\tau N_\tau} ,$$

where  $B$  is the baryon number and  $\Lambda_B^3$  denotes a spatial slice of the full set  $\Lambda_B$ .

The partition function Eq. (3.11) in terms of vertices for  $N_c = 3$  becomes

$$Z(\gamma, N_\tau) \stackrel{\gamma \rightarrow \infty}{=} \sum_{\mathcal{G}} e^{\mu_B B a_\tau N_\tau} \prod_{x \in \Lambda_M} v_\top^{n_\top(x)} v_\perp^{n_\perp(x)} , \quad \mu_B = 3\mu_q , \quad (3.13)$$

where  $\mathcal{G} = \{n_\top, n_\perp, B\}$  denotes the configuration space of all possible vertex configurations combined with static baryons. Fig 3.2 shows a possible configuration of a MDP system for  $N_\tau$  and  $\gamma$  large.

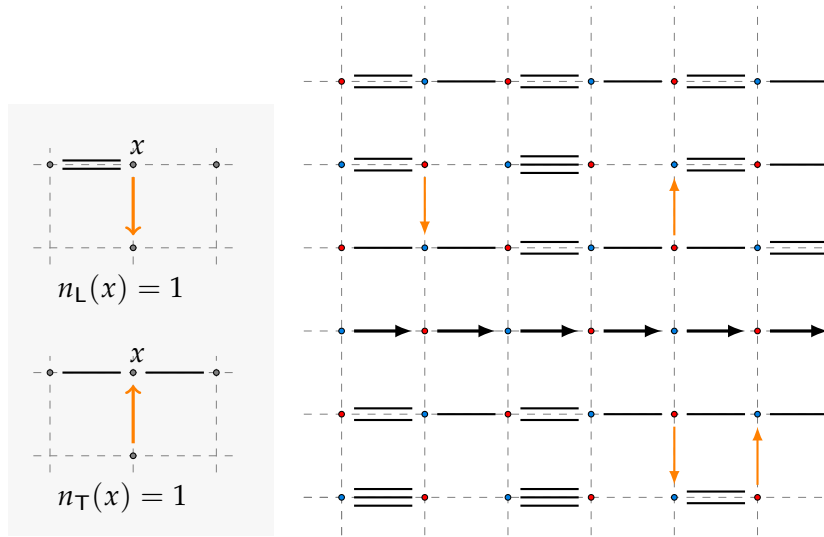


FIGURE 3.2: Graphical notation of the vertices (left) and example configuration in a 2-dimensional MDP discrete time system for  $\gamma$  and  $N_\tau$  large (right). The bipartite structure of the MDP-CT system is indicated by the red (emissions site) and blue (absorption site) colored sites. Oriented spatial dimers are indicated by orange arrows.

### 3.3.2 The $N_\tau \rightarrow \infty$ & $\gamma \rightarrow \infty$ limits

To eliminate the  $N_\tau$  and  $\gamma$  dependence in the  $N_\tau$  and  $\gamma$  limit we change the summation in Eq. (3.13) such that we can properly approximate the contributions in time direction using the following set of equivalence classes:

$$\Gamma_k \equiv \left\{ \mathcal{G}' \subset \mathcal{G} \mid n_{\vec{x}}(t) \sim n_{\vec{x}}(t') , k = \sum_x \frac{n_\top(x) + n_\perp(x)}{2} ; n_x, n_{x'} \in \mathcal{G}' , n_x \equiv n_{\top/\perp}(x) \right\} . \quad (3.14)$$

Thus,  $\mathcal{G}'$  denotes an equivalence class containing vertices equal up to time shifts and with a total number of  $k$  spatial dimers.

In the following step, we will introduce an auxiliary construction in order to estimate the number of possibilities to distribute spatial dimers at a dimer chain in a certain

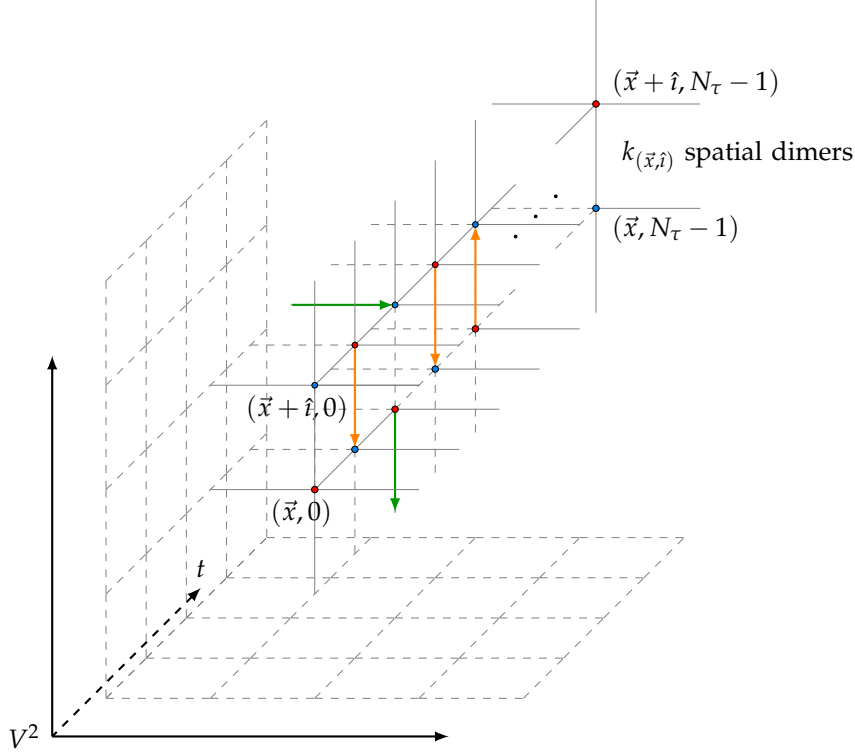


FIGURE 3.3: Schematic view on a cubic lattice, where only the time slices of the two spatial sites  $\vec{x}, \vec{x} + \hat{i} \in V^2$  are shown. The bipartite structure of the MDP-CT system is indicated by the colors red (emissions site) and blue (absorption site). Arrows symbolise emitted spatial dimers, where the green ones are connected with neighboring positions of  $\vec{x}$  or  $\vec{x} + \hat{i}$  omitting direction  $\hat{i}$  or  $-\hat{i}$ , respectively.

direction. The number of spatial dimers attached at a dimer chain in direction  $\hat{i}$  is given by  $k_{(\vec{x}, \hat{i})} \equiv \sum_{t=1}^{N_\tau} k_i(\vec{x}, t)$ , where  $k_i$  is the mesonic link variable from Sec. 3.1. We now argue that the number of available positions to distribute spatial dimers at is equal or even larger than

$$\left( \frac{N_\tau}{2} - K_{(\vec{x}, \hat{i})} \right) \equiv \left( \frac{N_\tau}{2} - \sum_{\pm \hat{j}, \hat{j} \neq \hat{i}} k_{(\vec{x}, \hat{j})} - \sum_{\pm \hat{j}, \hat{j} \neq -\hat{i}} k_{(\vec{x} + \hat{i}, \hat{j})} \right), \quad (3.15)$$

where the  $1/2$  factor is due to the even-odd decomposition and here we assume that spatial dimers from other directions fully take away possible positions.<sup>2</sup> It follows that in this case the number of possibilities to distribute all  $k$  spatial dimers is given by

$$\prod_{\vec{x} \in \Lambda_{M'}^3, \hat{i}} \left\{ \left( \frac{N_\tau}{2} - K_{(\vec{x}, \hat{i})} \right) \left( \frac{N_\tau}{2} - K_{(\vec{x}, \hat{i})} - 1 \right) \cdots \left( \frac{N_\tau}{2} - K_{(\vec{x}, \hat{i})} - k_{(\vec{x}, \hat{i})} \right) \right\} \\ \underset{N_\tau \rightarrow \infty}{\approx} \prod_{\vec{x} \in \Lambda_{M'}^3, \hat{i}} \left( \frac{N_\tau}{2} \right)^{k_{(\vec{x}, \hat{i})}} = \left( \frac{N_\tau}{2} \right)^k, \quad \text{with } k = \sum_{\vec{x} \in \Lambda_{M'}^3, \hat{i}} k_{(\vec{x}, \hat{i})}$$

<sup>2</sup>Which is in general not the case because spatial dimers coming from directions other than  $\hat{i}$  can share the same position (see Fig. 3.3), where here the word position rather denotes a slot to attach a spatial dimer at.

while letting  $N_\tau$  become large. We now make use of the fact that (3.15) is a lower bound of the true number of available positions. This includes that the true number of possibilities to distribute all spatial dimers admits the same limit  $(N_\tau/2)^k$ .

Hence, for large  $N_\tau$  the contributions in time direction for the set of equivalence classes  $\Gamma_k$  can be approximated by the factor  $(N_\tau/2)^k$  for a total number of  $k$  spatial hoppings. Finally, we pull out the  $\gamma^{-2k}$  factor of the product over the spatial hoppings (we remind that  $v_\top = \frac{2}{\sqrt{3}}\gamma^{-1} = \hat{v}_\top\gamma^{-1}$  and  $v_\perp = \gamma^{-1} = \hat{v}_\perp\gamma^{-1}$ ) and take the limits  $\gamma \rightarrow \infty$  and  $N_\tau \rightarrow \infty$ . Doing so, the continuous time partition function for  $N_c = 3$  is given by

$$\begin{aligned} \mathcal{Z}_{CT}(\mu_B, T) &= \sum_{k \in 2\mathbb{N}} \left( \frac{N_\tau}{2\gamma^2} \right)^k \sum_{g' \in \Gamma_k} e^{\mu_B B a_\tau N_\tau} \hat{v}_\top^{N_\top} \hat{v}_\perp^{N_\perp} \\ &= \sum_{k \in 2\mathbb{N}} \left( \frac{1}{2aT} \right)^k \sum_{g' \in \Gamma_k} e^{\mu_B B/T} \hat{v}_\top^{N_\top} \end{aligned} \quad (3.16)$$

We used the relations of  $N_\tau$  with the temperature given by  $a_\tau N_\tau = 1/T$  and  $N_\tau/\gamma^2 = 1/aT$ . The factor  $\kappa$  in  $N_\tau/\kappa\gamma^2 = 1/aT$  can be omitted by rescaling the temperature appropriately. The number of spatial hoppings are decomposed into  $k = (N_\top + N_\perp)/2$  with  $N_{\top/\perp} = \sum_x n_{\top/\perp}(x)$ . Note that we can now explicitly identify the baryon weighting  $e^{\mu_B B/T}$  in the new partition function. For more information see the article [1].



## Chapter 4

# Methods

### 4.1 The microcanonical density of states from the Wang-Landau method

In the following section the Wang-Landau method [2] is introduced which comprises substantial advantages over conventional approaches.

The general idea is that a modified random walk in the energy surface is employed in order to sample the microcanonical density of states  $\Omega(E)$  (DoS). Once the DoS is sampled, we can calculate various observables for arbitrary temperatures using that the canonical partition function is related to the microcanonical density by the following Laplace transformation

$$\mathcal{Z}(T) = \sum_E \Omega(E) e^{-E/kT} . \quad (4.1)$$

Compared to other Monte Carlo methods which directly sample in the canonical probability distribution the Wang-Landau method exhibits a huge advantage providing an exact expression of the partition function.

At the beginning of the simulation, the DoS  $\Omega_{WL}(E)$  is initialized with small values, e.g.  $\Omega_{WL}(E) = 1$  for all energies  $E$ . Starting from an arbitrary configuration with energy  $E$  we perform a random walk to propose a new configuration with energy  $E'$ ,<sup>1</sup> where the new energie  $E'$  is proposed with the implicit probability

$$P(E') = \frac{\Omega(E')}{\sum_E \Omega(E)} . \quad (4.2)$$

In the following, we adapt a Metropolis acceptance propabilty  $P_{accept}(E \rightarrow E')$  to the transition which is defined by

$$P_{accept}(E \rightarrow E') \equiv \min \left\{ \frac{\Omega_{WL}(E)}{\Omega_{WL}(E')}, 1 \right\} .$$

The transition probability then becomes

$$P(E \rightarrow E') \equiv P(E') P_{accept}(E \rightarrow E') = \frac{\Omega(E')}{\sum_E \Omega(E)} P_{accept}(E \rightarrow E') ,$$

We now modify  $\Omega_{WL}(E)$  or  $\Omega_{WL}(E')$ , if either the transition is rejected or accepted by multiplying the respective DoS with a modification factor  $f > 1$ . In addition, we

<sup>1</sup>Naturally, the random walk should be carried out in such a way that it reflects the desired probability distribution. As an example, to get the microcanonical DoS in a spin system such as the Ising model the random walk is realised by flipping the Ising spins.

increment the corresponding histogram  $H(E)$  at  $E$  or  $E'$  by 1 .<sup>2</sup>

Note that this updating scheme will take into account that, if the random walk proposes the energy  $E'$  more often than some other energy  $E$ , i.e.  $\Omega(E') > \Omega(E)$ , then transitions to  $E'$  become more unlikely accepted than transitions to  $E$ , so that we obtain  $\Omega_{WL}(E') > \Omega_{WL}(E)$ . Due to this dynamics of the algorithm it approaches detail balance up to an accuracy which depends on the modification factor  $f$

$$P(E \rightarrow E') \approx P(E' \rightarrow E) \quad .$$

Thus, if  $\Omega(E') > \Omega(E)$ , the acceptance probabilities become

$$P_{accept}(E \rightarrow E') = \frac{\Omega_{WL}(E)}{\Omega_{WL}(E')} \quad \wedge \quad P_{accept}(E' \rightarrow E) = 1$$

and we can directly write the transition probabilities as

$$\begin{aligned} P(E \rightarrow E') &\approx P(E' \rightarrow E) \\ \frac{\Omega(E')}{\sum_E \Omega(E)} \frac{\Omega_{WL}(E)}{\Omega_{WL}(E')} &\approx \frac{\Omega(E)}{\sum_E \Omega(E)} \\ \Leftrightarrow \frac{\Omega_{WL}(E)}{\Omega_{WL}(E')} &\approx \frac{\Omega(E)}{\Omega(E')} \quad . \end{aligned}$$

For the case  $\Omega(E') < \Omega(E)$  the proof is analog. Hence, the ratio of the DoS converges to the true ratio with an error in the accuracy proportional to  $\ln(f)$  considering the exponent.

In order to get a better accuracy the modification factor  $f$  should be reduced, for which we additionally sampled the histogram  $H(E)$ . Due to the detailed balance property this histogram flattens up to a difference proportional to the ratio  $\Omega(E)/\Omega(E')$  of the densities. We now define a flatness condition by the margin  $\delta$  of the mean  $\bar{H} = 1/N \sum_E H(E)$ ,  $N$  being the number of energies, which should not be exceeded by  $|H(E) - \bar{H}|$  for every energy  $E$ . Every time this condition is fulfilled, we reduce the modification factor, reset all histogram entries to zero and continue the algorithm with a finer accuracy. The modification of  $f$  should follow a recipe which decreases  $f$  in order to approach 1 relatively fast. Doing so, the simulation is finished, if  $f$  is smaller than some value  $f_{final}$ .

Note, the margin  $\delta$  and  $f_{final}$  serves as control parameter whereas the former controls how long  $\Omega_{WL}$  is modified for a given  $f$  and the latter determines at which accuracy level we want to stop. We should also consider to choose  $f$  large enough to quickly reach all possible energies.

Once the simulation is done, we want to extract the approximation for the DoS  $\Omega(E)$  out of  $\Omega_{WL}(E)$ . Since the ratio  $\Omega_{WL}(E)/\Omega_{WL}(E')$  converges to the true ratio  $\Omega(E)/\Omega(E')$  we can argue that the sampled DoS  $\Omega_{WL}(E)$  approximates  $\Omega(E)$  up to some factor  $C$ . Thus, we have

$$\Omega_{WL}(E) \approx C \Omega(E) \quad , \quad \forall E \quad (4.3)$$

<sup>2</sup>Obviously, if we perform the random walk without the acceptance probability, accepting all energies immediately, the normalized histogram  $H(E)/\sum_E H(E)$  would converge to the DoS  $\Omega(E)$ . If we do so, we have to keep in mind that the number of sweeps  $\sum_E H(E)$  have to be a multiple of the number of all possible configurations in order to get a good accuracy which makes this method highly inefficient.

The factor  $C$  can be obtained by using the knowledge about  $\Omega(E)$  in the ground state  $E_0$ . Hence,

$$\begin{aligned}\Omega_{WL}(E_0) &= C \Omega(E_0) \\ \Leftrightarrow C &= \frac{\Omega_{WL}(E_0)}{\Omega(E_0)}\end{aligned}\quad (4.4)$$

Substituting Eq. (4.4) into Eq. (4.3) and solving for  $\Omega(E)$  we get the following formula to get the approximation of the true DoS:

$$\Omega(E) \approx \frac{\Omega(E_0)}{\Omega_{WL}(E_0)} \Omega_{WL}(E) \quad .$$

Due to the fact that the energy range scales with the size of the system, it is recommended to perform the algorithm within parts of the whole range. In this case we have to adjust  $\Omega_{WL}(E)$  to the respective boundary states. Note that it suffices to sample within the first half of the total energy range, if the DoS is symmetric.

To circumvent storing extremely large numbers the logarithmic DoS should be updated instead. The update scheme then turns to

$$\ln(\Omega_{WL}(E)) \rightarrow \ln(\Omega_{WL}(E)) + \ln(f)$$

and the recipe to extract the approximation of  $\ln(\Omega(E))$  becomes

$$\ln(\Omega(E)) \approx \ln(\Omega_{WL}(E)) - \ln(\Omega_{WL}(E_0)) + \ln(\Omega(E_0)) \quad .$$

## 4.2 The Wang-Landau algorithm applied to the Ising model

To test the Wang-Landau algorithm, it is applied to the Ising model for dimensions  $d = 2, 3$  and constrained to nearest neighbor interaction. In the following the Wang-Landau method is compared with other Monte Carlo methods by considering the results for the energy expectation values for various temperatures.

The Hamiltonian of the  $d$ -dimensional Ising model without an external field is given by

$$H = J \sum_{\langle i,j \rangle} s_i s_j \quad (4.5)$$

with the exchange energy  $J$  and the spin variable  $s_i \in \{-1, 1\}$ . The  $\langle i, j \rangle$  denotes the sum over nearest neighbor interaction. The modification factor is initialized with  $f = e^1$  and we will reduce it by applying the square root every time the flatness condition is fulfilled. The DoS is set to  $\Omega_{WL}(E) = 1$  for all energies. The flatness condition  $\delta$  have to be appropriately chosen for the given energy range in order to keep the algorithm running long enough even within small ranges. It should be defined as some percentage of the mean  $\bar{H}$ . In order to calculate a statistical error the density can be sampled various times. For the precision we choose  $f_{final} = \exp(10^{-8})$  and for one simulation we go through the following steps:

1. Choose a random lattice configuration  $\sigma$  and compute the energy  $E_{old}$  with Eq.(4.5).
  - (a) By flipping the spin on a randomly chosen site a new configuration with energy  $E_{new}$  is proposed.

- (b) Perform the Metropolis acceptance step. So check if  $p < P_{accept}(E_{old} \rightarrow E_{new}) = \min \left\{ \frac{\Omega_{WL}(E_{old})}{\Omega_{WL}(E_{new})}, 1 \right\}$  with probability  $p \in (0, 1)$ :  
 If accepted update as follows:
  - $H(E_{new}) \rightarrow H(E_{new}) + 1$
  - $\ln(\Omega_{WL}(E_{new})) \rightarrow \ln(\Omega_{WL}(E_{new})) + \ln(f)$
  - and set  $E_{old} = E_{new}$ .
 Else update:
  - $H(E_{old}) \rightarrow H(E_{old}) + 1$
  - $\ln(\Omega_{WL}(E_{old})) \rightarrow \ln(\Omega_{WL}(E_{old})) + \ln(f)$
  - and return to previous configuration  $\sigma$ .
 (c) Check if flatness condition is reached.  $H(E)$  should fulfill  $\delta > |\bar{H} - H(E)|$  for every  $E$ :<sup>3</sup>  
 If true reset the histogram  $H(E)$  and continue with 2.  
 Else return to step 1a).
2. Reduce the modification factor according to  $f \rightarrow \sqrt{f}$  and check if  $f < f_{final}$ :  
 If true continue with 3.  
 Else return to step 1a).
3. Leave the loop, normalize  $\ln(\Omega_{WL}(E))$  by subtracting for every energy  $E$  with  $\min_E \{\ln(\Omega_{WL}(E))\}$  and adjusting the result to the ground state.

To compare the Wang-Landau algorithm with Monte Carlo algorithms which sample through the canonical distribution we perform various simulations for a square lattice of size  $V = 8^2$  and a cubic lattice of size  $V = 4^3$ . Once we have sampled the DoS, we can use Eq. (4.1) to calculate the energy expectation value via the formula

$$\langle E \rangle_T = -\frac{\partial \ln(\mathcal{Z}(T))}{\partial \beta} \quad , \quad \mathcal{Z}(T) = \sum_E \Omega(E) e^{-E/kT}$$

where  $\beta = 1/kT$ . The expectation value for energy  $E$  is then

$$\langle E \rangle_T = \frac{\sum_E E \Omega(E) e^{-\beta E}}{\sum_E \Omega(E) e^{-\beta E}} \quad .$$

In Fig. 4.1 and 4.2 the results of both simulations for square and cubic lattices, are plotted with roughly same number of sweeps ( $\sim 10^9$ ). We can observe that the accuracy decreases, if the number of updates relaxes to a larger energy range. If we choose a higher precision and smaller flatness condition, the error can be further decreased which on the other hand leads to more calculation time. However, the advantage of the Wang-Landau method is that once we have generated  $\Omega_{WL}(E)$ , we can calculate observables for arbitrary temperatures. If we now choose an arbitrary fine temperature cut-off, we can find pseudocritical points with high precision such that very accurate extrapolations can be done (see section 4.4), whereas other Monte Carlo methods require many simulations to achieve that.

<sup>3</sup>In practice this should be done after a certain amount of sweeps depending on the size of the lattice to save computation time.

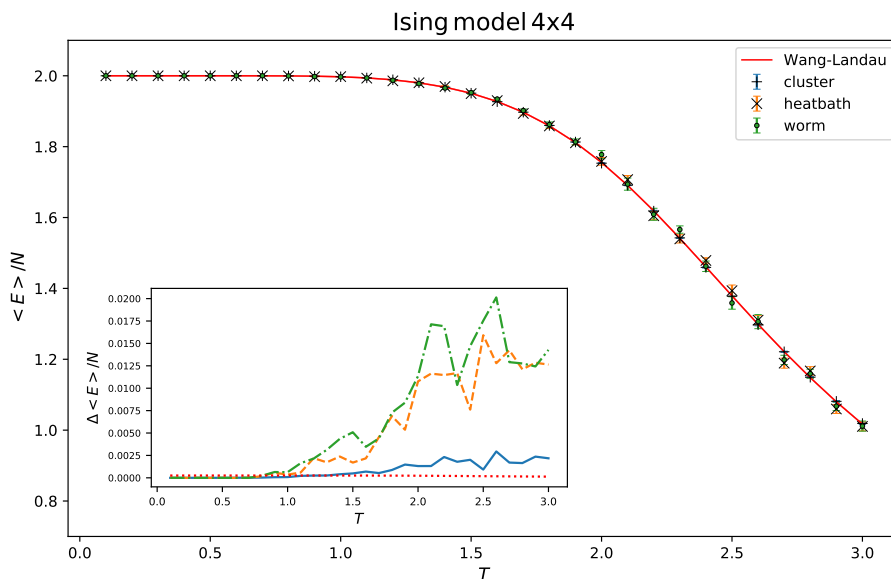


FIGURE 4.1: The solid line shows the resulting energy expectation value by using the density of states  $\Omega(E)$  of a square lattice of size  $L = 4$  in the Ising model generated via the Wang-Landau method. For comparison the results for the cluster/heatbath/worm algorithm [14] using the software package ARIADNE, developed by Unger et al, are shown.

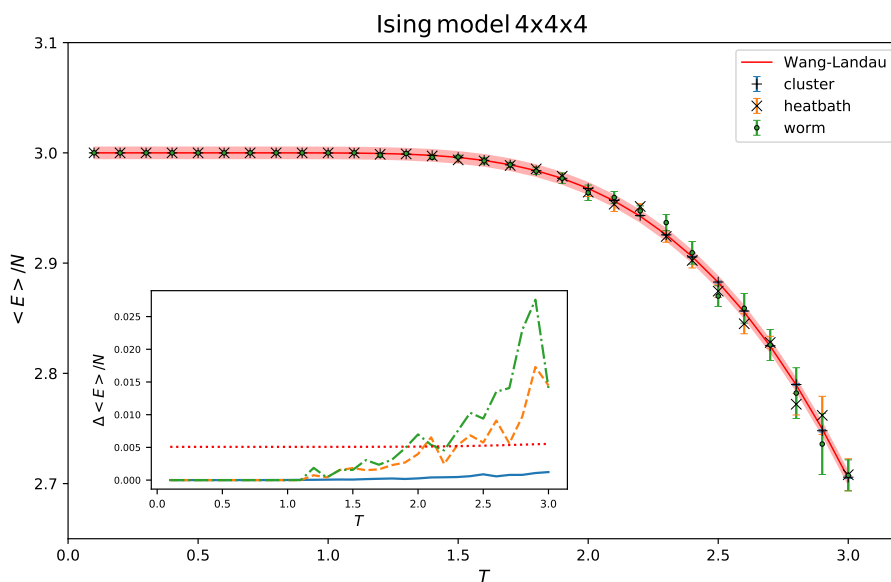


FIGURE 4.2: The solid line shows the resulting energy expectation value by using the density of states  $\Omega(E)$  of a cubic lattice of size  $L = 4$  in the Ising model generated via the Wang-Landau method. For comparison the results for the cluster/heatbath/worm algorithm [14] using the software package ARIADNE, developed by Unger et al, are shown.

### 4.3 Finite-Size Scaling

For a finite Ising system the specific heat does not diverge as well as the peak locations are slightly shifted (see Fig. 4.4). Such finite size effects arise from the fact that the correlation length  $\xi$  of the system is prevented from becoming larger than  $\xi \approx L$ . At this point, the system of size  $L^d$  already becomes effectively ordered, where  $d$  is the dimension. On infinite scale the correlation length diverges near the critical point and follows some power law

$$\xi \propto |t|^{-\nu} \quad ,$$

where

$$t \equiv T - T_c$$

is the reduced temperature. For a finite sized system, the correlation length reaches its maximum  $\xi \approx L$  for  $T$  approaching  $T_c$  and we get

$$\xi \approx L \propto |T_L - T_c|^{-\nu} \quad , \quad (4.6)$$

where  $T_L$  is the pseudocritical point for which we obtain the proportionality to  $\xi \approx L$ . We now consider the specific heat near the critical temperature which also obeys a power law

$$C_V(T) = \frac{\langle E^2 \rangle_T - \langle E \rangle_T^2}{T^2} \propto |T - T_c|^{-\alpha} \quad , \quad (4.7)$$

where  $\alpha$  is the critical exponent for the specific heat. Following the same argument as above, we assume that for some pseudocritical point the maximum of the specific heat will be attained in a finite sized system. It turns out that it can be identified with the same  $T_L$ . Hence,

$$C_{V,max} \propto |T_L - T_c|^{-\alpha} \quad . \quad (4.8)$$

Combining Eq. (4.6) and Eq. (4.8) we obtain

$$C_{V,max} \propto |T - T_c|^{-\alpha} \propto L^{\frac{\alpha}{\nu}} \quad .$$

Rewriting this we get

$$T_L - T_c = \text{const} \cdot L^{-\frac{1}{\nu}} \equiv c \cdot L^{-\frac{1}{\nu}} \quad . \quad (4.9)$$

So in order to get the critical exponent  $\nu$  we have to apply a power law fit using the pseudocritical points  $T_L$  from different maxima of the specific heat  $C_V$ . For more details see [15].

### 4.4 Finite-Size scaling applied to the Ising model

In this section finite size scaling is done in order to obtain the critical temperature of the 2D Ising model. Here, we take advantage of the density of states, generated via the Wang-Landau method, in order to calculate the specific heat and determine the peak locations with high precision.

In the following the, DoS  $\Omega_{WL}(E)$  is sampled for the lattice volumes  $V = 16^2, 32^2$  and  $50^2$  (see Fig. 4.3). Note, in the 2D Ising model it is possible to compare the

data with the exact solution of the DoS provided by [16]<sup>4</sup>, where the relative error/deviation is given by  $\epsilon(X) = |(X - X_{exact})/X_{exact}|$ . In Tab. 4.1, the maximal relative error and the number of sweeps for each volume is listed. We have chosen appropriately small flatness conditions for smaller lattice sizes such that the algorithm is modifying the respective densities long enough. We now choose a temper-

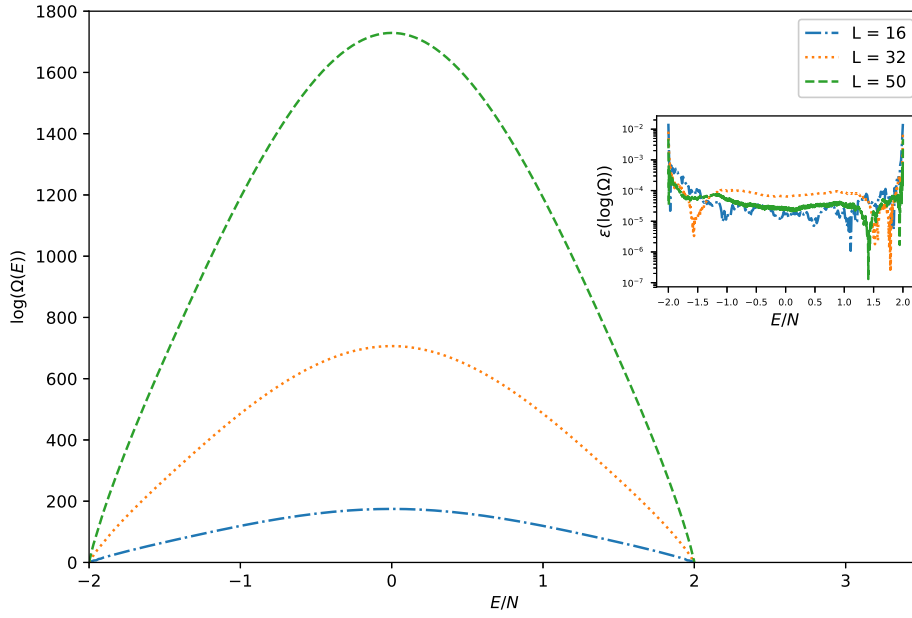


FIGURE 4.3: The density of states for 2D Ising model from the Wang-Landau method compared to the exact data from [16]. Because the data for both results coincides the relative error  $\epsilon(X) = |(X - X_{exact})/X_{exact}|$ , where  $X = \log(\Omega_{WL}(E))$ , is shown in the inset figure. Note the normalized energy range  $E/N \in [-2, 2]$  is considered to compare different volumes  $V = L \times L$ .

$L$	$\delta/\bar{N}$	$\epsilon_{max}[in\ %]$	#Sweeps
16	0.01	0.9	$2 \times 10^8$
32	0.05	1.2	$5 \times 10^9$
50	0.1	0.5	$7 \times 10^9$

TABLE 4.1: Relative error of Wang-Landau simulated densities with respect to exact data in a 2D Ising model for different  $L \times L$  volumes.

ature cut-off  $\{T_1, T_2 | \Delta T = 0.0001\}$ ,  $\Delta T$  denoting the step size, and compute specific heat  $C_V$  for every temperature step using

$$C_V(T) = \frac{\langle E^2 \rangle_T - \langle E \rangle_T^2}{T^2} . \quad (4.10)$$

<sup>4</sup>The Mathematica program which is proposed here is restricted up to  $L = 50$ .

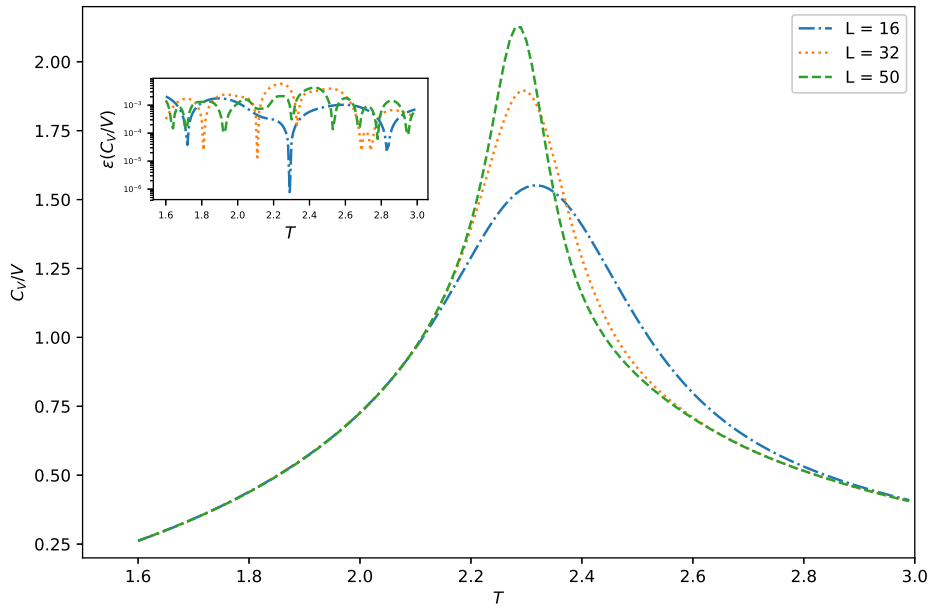


FIGURE 4.4: Normalized specific Heat  $C_V$  with relative error  $\epsilon(X) = |(X - X_{exact})/X_{exact}|$  (inset figure), where  $X_{exact}$  is calculated via Eq. (4.10) using the exact DoS from [16], for 2D Ising model and different volumes  $V = L \times L$ .

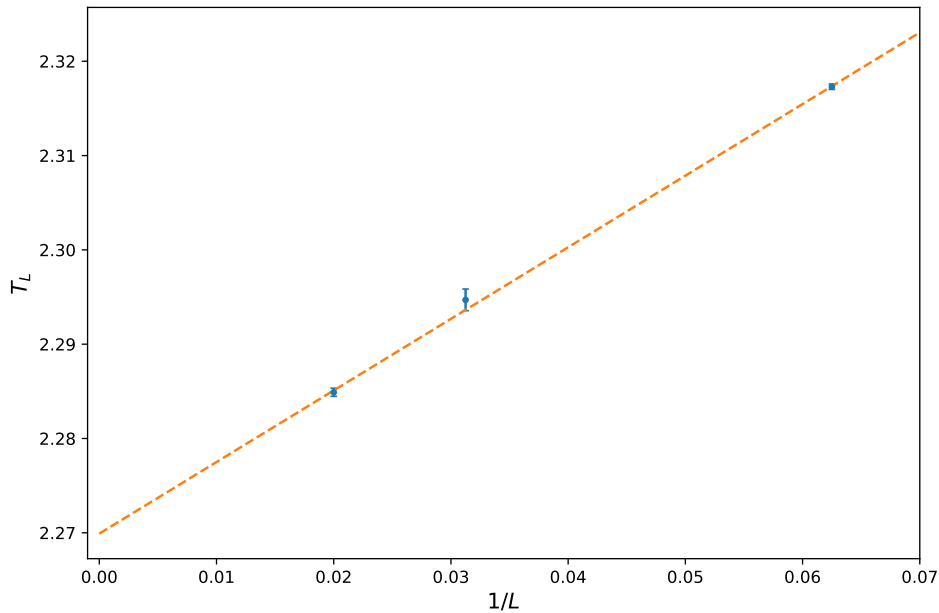


FIGURE 4.5: Power law fit using  $T_L = T_c + c \cdot L^{-1/\nu}$  with  $\nu = 1$  and pseudo-critical points  $T_L$  obtained from the specific heat using the DoS, generated via the Wang-Landau method in the 2D Ising model.

Comparing the data with the exact result (see Fig. 4.4) the error within all data points is not bigger than 0.58%.

In order to apply finite size scaling, the peak locations  $T_L$  of the specific heat are identified for the distinct lattice volumes (see Sec. 4.3). The fit, see Eq. (4.9), has three parameters  $T_c$ ,  $c$  and  $\nu$ , where we have for the critical exponent  $\nu = 1$  in the 2D Ising model. Performing the error weighted fit using the pseudocritical points  $T_L$ , we obtain  $T_c = 2.2699(9)$  which is close to the literature value of  $T_c = 2.2691$ .

## 4.5 The worm algorithm in SC-QCD

To generate configurations according to the distribution of a system, described by Eq. (3.9), Monte Carlo techniques such as the *directed path algorithm* (dpa) from [17] can be used. The dpa is essentially a worm algorithm with the feature that backtracking is not allowed.

In the MDP system the worm is split in two different updates in order to update the mesonic and baryonic part independently. Before going through the worm updates in more detail, we discuss an interesting feature when changing into the dual representation with the new variables  $k_{\hat{\mu}}$ ,  $b_{\hat{\mu}}$  and  $n_M$ . In this picture the partition function (3.9) can be decomposed in two parts by extending the parameter set on every site  $x$  to all directions ( $n_M, k_{\hat{\mu}}, b_{\hat{\mu}}, \hat{\mu} = \pm\hat{0}, \dots, \pm\hat{3}$ ). Thus, we can rewrite the partition function into

$$\mathcal{Z} = \sum_{\{n_M, k, b\}} \prod_{\{x_a\}} W_a(x_a) \prod_{\{x_p\}} W_p(x_p) \sigma(n_M, k, b) \quad (4.11)$$

with

$$W_a(x) = \prod_{\hat{\mu}=\pm\hat{0}, \dots, \pm\hat{3}} \left( \frac{(N_c - k_{\hat{\mu}})!}{N_c! k_{\hat{\mu}}!} e^{3b_{\hat{\mu}}(\delta_{\hat{\mu}, \hat{0}} + \delta_{\hat{\mu}, -\hat{0}}) a_{\tau} \mu_q} \right) \frac{N_c!}{n_M(x)} (2am_q)^{n_M(x)} \quad (4.12)$$

and

$$W_p(x) = \prod_{\hat{\mu}=\pm\hat{0}} \left( \gamma^{2k_{\hat{\mu}}+3|b_{\hat{\mu}}|} \right) \frac{N_c!}{n_M(x)!} (2am_q)^{n_M(x)} \quad (4.13)$$

Now the lattice is split in two separate set of sites, the active sites  $\{x_a\}$  and the passive sites  $\{x_p\}$ . Using the bipartite representation Eq. (4.11) the worm update scheme consists of active site updates and passive site updates.

Starting with the mesonic update, a worm head and tail in form of monomers is introduced on a site which is connected to at least one dimer violating the constraint Eq. (3.6). Per definition, this site is active. In the following, the worm head moves through passive (active) sites restoring (violating) the constraint Eq. (3.6) by removing (producing) dimers in turns until the worm head removes a monomer on an active site. Note, in the chiral limit the worm head propagates through the lattice until the tail is removed. During the update worm estimators are accumulated every time the worm performs passive site updates.

In contrast to the mesonic update, the worm head and tail of the baryonic worm is placed either on a baryonic site or on a site with a triple dimer attached. The worm head propagates through the lattice accepting only sites connected with either baryonic links or a triple dimer converting them into each other, respectively. The baryonic update is finished when the worm head removes the tail.

Updating in this way, every possible configuration can be reached and ergodicity is fulfilled. Both, the mesonic- and the baryonic worm, satisfy the detailed balance condition

$$W(C)P(C'|C) = W(C')P(C|C') \quad ,$$

where  $W(C) = \prod_{x_a} W_a(x_a) \prod_{x_p} W_p(x_p)$  is the weight of the worm configuration  $C$  and  $P(C|C')$  is the transition probability from configuration  $C$  to  $C'$ . A detailed proof can be found in [4]. Note, that this algorithm does not suffer from critical slowing down for small masses like it was the case for the MDP-update used in [11], whose efficiency was dependent on the quark mass.

## 4.6 Worm algorithm in CT-limit

In order to generate configurations in the mesonic part of the continuous time system, described by Eq. (3.16), we will use a worm-type algorithm similar to the directed path algorithm mentioned in Sec. 4.5. Similar to the bipartite lattice in the dual representation the lattice in the continuous time limit can be decomposed into emission- and absorption sites. Again, the mesonic- and baryonic part are treated independently.

Initially, the worm head and tail are located at an absorption site and violate the constraint Eq. (3.6). Subsequently, the worm head propagates through the lattice restoring (violating) the constraint every time it visits emission (absorption) sites. The algorithm either stops at an absorption site connected to a spatial dimer which is then deleted or generates a spatial dimer at an emission site. The typical distance at which a spatial dimers is emitted is given by the Poisson process

$$P(\Delta\beta) = \exp(-\lambda\Delta\beta) \quad ,$$

where

$$\Delta\beta \in [0, \beta = 1/aT] \quad \text{and} \quad \lambda = d_M(x, t)/4 \quad , \quad d_M(x, t) = 2d - \sum_{\mu} n_B(x + \hat{\mu}) \quad .$$

The ‘‘Decay constant’’  $\lambda$  for spatial dimer emissions is space-time dependent when baryons are present. The dependence is given by  $d(x, t)$  which is the number of mesonic neighbors at a given coordinate.

Thus, the Poisson process assures that the spatial dimers are exponentially distributed. Other than in the directed path algorithm there is no need for a baryonic worm. Positive- and negative oriented static baryons can be exchanged with static mesonic lines without any spatial dimer attached. The Wang-Landau method, see next section (Sec. 4.7), used in this thesis will take care of these updates.

## 4.7 The Wang-Landau applied to the MPD-CT model

In chapter 3 section 3.3 a new representation of the partition function given by Eq. (3.16) was established in the continuous time limit of the MDP (MDP-CT) model. The exponential  $e^{\mu_B B/T}$  can be identified as the integral kernel of a Laplace transformation in the baryon number  $B$ . We now rewrite the sum using the canonical DoS  $g(B, T)$  for fixed  $B$  and  $T$ . It follows that the grand canonical representation Eq. (3.16)

admits the Laplace transformation of canonical DoS:

$$\mathcal{Z}(\mu_B, T) = \sum_{B=-V}^V g(B, T) e^{\mu_B B/T} \quad , \quad V = |\Lambda^3| \quad . \quad (4.14)$$

Due to the fact that baryons become static in the continuous time limit the Wang-Landau method, introduced in Sec. 4.1, can be adapted to obtain the set  $\{g(B, T)\}_B$  which is the subject of this section.

To sample DoS  $g(B, T)$  we employ the Wang-Landau method to closed loop configurations, yielded by mesonic worm updates (Sec. 4.6). In this case the sampling would be done in the baryon number which is given by  $B = B^+ - B^-$ , where  $B^+$  and  $B^-$  denotes baryons and anti-baryons. However, it is more efficient to keep track of the resummation  $P = B^+ + B^-$  which we refer to as polymer number. The advantage is that sampling in the number of blocking polymers  $P \in \{0, V\}$  requires only half of the simulation range of the baryon number  $B \in \{-V, V\}$ . Another benefit is that analytical cross-checks in the large temperature limit can easily be done.

The weight of a configuration with  $P$  polymers is given by  $\omega(P) = (2 \cosh(\mu_B/T))^P$  and is related to the baryon weight by a *binomial transformation*:

$$\begin{aligned} w(P, \mu_B/T) &= \left( e^{\mu_B/T} + e^{-\mu_B/T} \right)^P \\ &= \sum_{B^+=0}^V \binom{P}{B^+} e^{\mu_B B^+/T} e^{-\mu_B (P-B^+)/T} \\ &= \hat{w}(P) e^{\mu_B B/T} \end{aligned}$$

using that  $B^- = P - B^+$ . The DoS  $g(B, T)$  in the baryon number  $B$  can be obtained via the convolution

$$\begin{aligned} \sum_{P=0}^V g(P, T) w(P, \mu_B/T, B) &= \sum_{P=0}^V g(P, T) \hat{w}(P, B) e^{\mu_B B/T} \\ &= g(B, T) e^{\mu_B B/T} \quad , \end{aligned} \quad (4.15)$$

where polymer weight  $g(P, \mu_B/T, B)$  is restricted to a fixed baryon number  $B = B^+ - B^- = 2B^+ - P$ . The same holds for the binomial transformation. Hence,

$$\hat{w}(P, B) = \sum_{\substack{B^+=0 \\ B=2B^+-P}}^V \binom{P}{B^+} \quad .$$

In the following, the sampling of the density  $g(P, T)$  can be realised by simply performing the mesonic worm and Wang-Landau updates in turns. In more detail, after every mesonic worm update we loop through the volume and propose changes in the state of static sites <sup>5</sup>, accepting these with a Wang-Landau probability given by

$$p_{\text{accept}}(P_{\text{old}} \rightarrow P_{\text{new}}) = \min \left\{ \frac{g_{\text{WL}}(P_{\text{old}}, T)}{g_{\text{WL}}(P_{\text{new}}, T)}, 1 \right\} \quad ,$$

<sup>5</sup>Static sites can admit either  $N_c + 1$  possible mesonic states or the polymer state. If we would sample in the baryon number  $B$ , we have to distinguish between the baryon and anti-baryon states.

while accepting dynamic sites immediately since  $P_{old} = P_{new}$  holds. The state density  $g_{WL}(P, T)$  is initialized with small values and, analog to Sec. 4.1, we switch to a logarithmic updating scheme. After choosing an arbitrary configuration with polymer number  $P$ , the simulation consists of the following steps:

1. A mesonic worm update is carried out and subsequently a loop through the volume is started:
  - If the site is static (no spatial dimer attached), a new state out of  $N_c + 2$  possible states is proposed. Thus, the polymer number becomes  $P \rightarrow P + dP$ , where the change is  $dP = 0, \pm 1$  for the cases if we interchange either two mesonic states, a mesonic state with a polymer or the reverse, respectively. The proposal is accepted if  $p < \min\left\{\frac{g_{WL}(P, T)}{g_{WL}(P+dP, T)}, 1\right\}$  for some random number  $p \in (0, 1)$ :
    - If accepted:
      - $H(P + dP) \rightarrow H(P + dP) + 1$
      - $\ln(g_{WL}(P + dP, T)) \rightarrow \ln(g_{WL}(P + dP, T)) + \ln(f)$
    - Else reject new state and update:
      - $H(P) \rightarrow H(P) + 1$
      - $\ln(g_{WL}(P, T)) \rightarrow \ln(g_{WL}(P, T)) + \ln(f)$
  - Otherwise immediately update  $\ln(g_{WL}(P, T)) \rightarrow \ln(g_{WL}(P, T)) + \ln(f)$  and  $H(P) \rightarrow H(P) + 1$ .
2. Check if the flatness condition is reached.  $H(P)$  should fulfill  $\delta > |\bar{H} - H(P)|$  for every  $P$ :
  - If true reset the histogram  $H(P)$  and continue with 3.
  - Else repeat step 1.
3. Reduce the modification factor according to  $f \rightarrow \sqrt{f}$  and check if  $f < f_{final}$ :
  - If true terminate the simulation and normalize  $\ln(g_{WL}(P, T))$ .
  - Else return to step 1.

To get the approximated  $g(P, T)$  we use the recipe proposed in section 4.1 using that for the ground state  $P = V$  (hence all sites are occupied by polymers) we simply have  $g(V, T) = 1$ . A statistical error can be calculated by performing various simulations for  $g(P, T)$ .

The DoS is an important tool since we can use it to investigate the grand canonical probability distribution for  $\mu_B \neq 0$  from which we can get information about the phase boundaries at the first order nuclear transition (see Sec. 5).

## Chapter 5

# Results

In this thesis we aim for the sampling of the canonical density of states (DoS) in a MDP-CT system with the  $SU(3)$  gauge group using the Wang-Landau method combined with the worm algorithm (see Sec. 4.7). In the first section the results are cross-checked for a spatial volume of size  $V = 4^3$  to assure validity. We proceed with calculating the canonical DoS for different lattice volumes. Doing so we can study the double peak structure of the grand canonical probability density in thermodynamic limit  $V \rightarrow \infty$ . In more detail, by identifying the peak locations for different lattice extents we detect the boundaries of the mixed phase in the canonical phase diagram. Using finite size scaling will yield the peak locations, hence the phase boundaries of the mixed phase, in the limit ( $V \rightarrow \infty$ ) of continuous time lattice SC-QCD.

### 5.1 Cross-checks

In this section the binomial transformation between the polymer and baryon DoS is investigated. We considered a MDP-CT system with a spatial volume of size  $V = 4^3$ . Furthermore, the obtained results for the expected polymer and baryon number are compared with data sampled through important sampling of closed loop configurations generated by mesonic worm and additional baryon updates [1].

The DoS  $g(P, T)$  is sampled in the polymer resummation  $P = B^+ + B^-$  for various temperatures (Fig. 5.1) following the steps, described in Sec. 4.7. We used for the precision a limit of  $f_{final} = 10^{-8}$  and a flatness condition of  $\delta = 0.05 \cdot \bar{H}$ . In the following, the DoS  $g(B, T)$  in the baryon number can be obtained by using the binomial transformation from Eq.( 4.15). In order to verify the binomial transformation, we also sample the density  $g(B, T)$  directly in the baryon number. The deviation of both results is shown in the inset of Fig. 5.2. Note that the error does not exceed 0.17% which assures that the binomial transformation between the densities in  $B$  and  $P$  is correct.

To conclude this section, the resulting expectation values for the polymer and baryon densities for temperatures down to  $aT = 1.0$  are compared with the results, obtained through important sampling of configurations generated via mesonic worm updates and subsequent baryon updates. The expected baryon density is given by

$$\langle B/V \rangle = \frac{\sum_B B/V g(B, T) w(B, \mu_B/T)}{\sum_B g(B, T) w(B, \mu_B/T)}, \quad w(B, \mu_B/T) = e^{\mu_B B/T} \quad (5.1)$$

for fixed temperature  $T$  and chemical potential  $\mu_B$ , whereas the expected polymer density can be calculated by substituting  $g(P, T)$  and  $w(P, \mu_B/T) = (2 \cosh(\mu_B/T))^P$

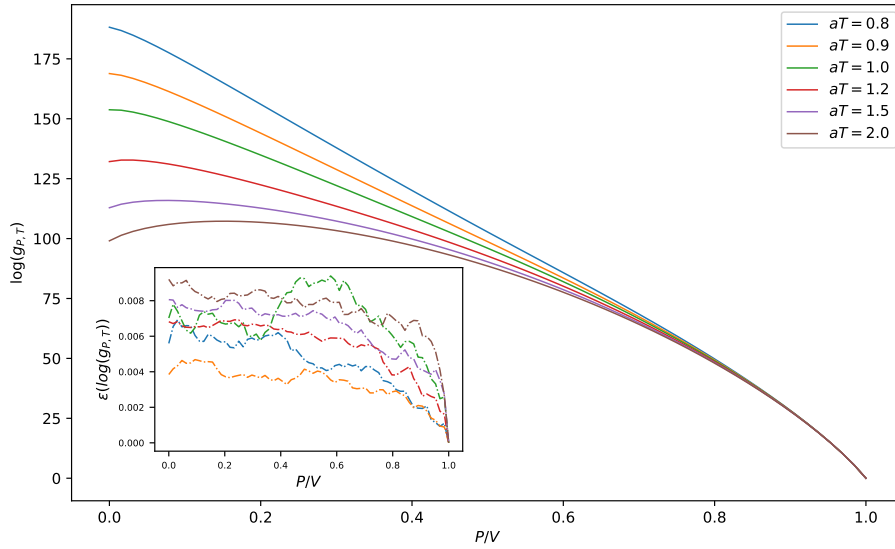


FIGURE 5.1: Logarithmic density of states  $g(P, T)$  of a MDP-CT system of size  $V = 4^3$  in the polymer resummation  $P = B^+ + B^-$  for different temperatures. The statistical error for 10 simulations of  $g(P, T)$  is small, and is hence shown in the extra inset figure. The color for the respective temperature coincides for both figures.

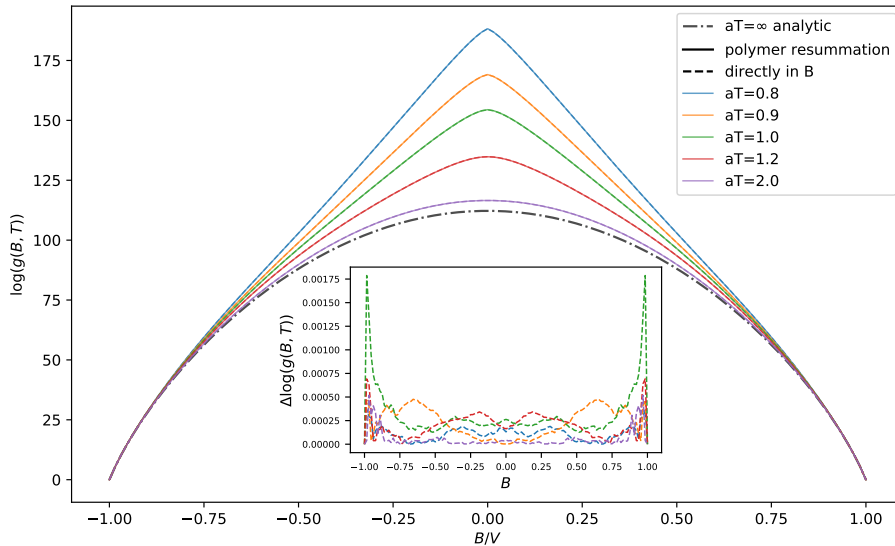


FIGURE 5.2: The density of states  $g(B, T)$  of a MDP-CT system of size  $V = 4^3$ , sampled directly in the baryon number  $B$  (dashed lines), is compared with  $g(B, T)$ , obtained through the binomial transformation (Eq. 4.15) of  $g(P, T)$  (solid lines). The deviation is shown in the inset figure since the data for both, simulations in  $B$  and  $P$ , is indistinguishable. The analytic result refers to appendix B.

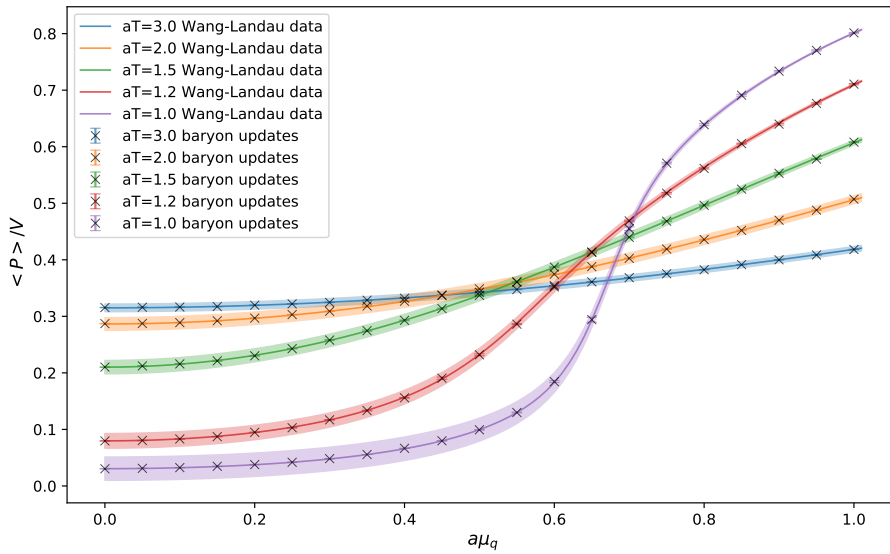


FIGURE 5.3: The solid lines shows the resulting expected polymer density using the density of states  $g(P, T)$  of a MDP-CT system of size  $V = 4^3$ , generated with the Wang-Landau method. For comparison, the Wang-Landau data is plotted against results, obtained by important sampling of configurations generated via mesonic worm and additional baryon updates.

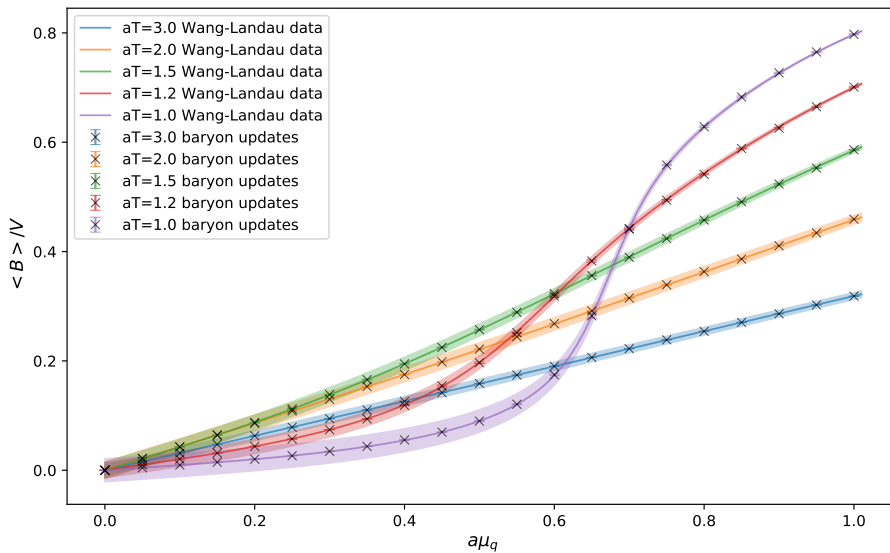


FIGURE 5.4: The solid lines shows the resulting expected baryon density using the density of states  $g(P, T)$  of a MDP-CT system of size  $V = 4^3$ , generated with the Wang-Landau method. For comparison, the Wang-Landau data is plotted against results, obtained by important sampling of configurations generated via mesonic worm and additional baryon updates.

in Eq. (5.1). In Fig. 5.3 and 5.4, we can observe that the Wang-Landau result matches with the important sampling data with high precision.

## 5.2 Grand canonical and canonical phase diagram in SC-LQCD

To study the grand canonical and canonical phase diagram in continuous time SC-LQCD in the limit  $V \rightarrow \infty$  we consider the grand canonical probability density which is given by

$$p(\mu_q, T, B) = g(B, T) e^{3\mu_q B/T} / \mathcal{Z}(\mu_q, T), \quad \mathcal{Z}(\mu_q, T) = \sum_{B=-V}^V g(B, T) e^{3\mu_q B/T}. \quad (5.2)$$

The DoS is generated in the polymer resummation  $P$  and we calculate  $g(B, T)$  via the binomial transformation. Hence, we can cover the canonical phase diagram in the baryon and polymer density, while performing simulations only for  $P$ .

The advantage of the Wang-Landau method is that we first obtain the canonical DoS  $g(B, T)$  in order to evaluate (5.2). Thus, it does not only avoid many simulations for chemical potentials  $a\mu_q$  near the phase transition because of the exact expression, but also overcomes slow kinetics when directly sampling in  $p(\mu_q, T, B)$  near  $a\mu_c(T)$ . Note that we express the temperature and chemical potential in dimensionless lattice units, where for the temperature a rescaling with  $\kappa$  is needed (see Sec. 3.3). For simplicity we omitted the rescaling in future calculations.

Due to the first order phase transition at  $a\mu_c(T)$  the grand canonical probability distribution is expected to admit a steep double peak structure, when considering the thermodynamic limit. This characteristic double peak structure corresponds to the split of the phase boundary below the tricritical point in the canonical phase diagram exhibiting the coexistence phase, where the peak locations  $n_{B,c}^{(1)}$  and  $n_{B,c}^{(2)}$  reflect its boundaries.

In the finite sized MDP-CT system instead we rather observe a softened double peak structure at a deviating pseudocritical point  $a\mu_L(T)$  caused by finite size effects.

In the following, the grand canonical probability distribution (Eq. 5.2) is scanned in  $a\mu_q$  using some arbitrary small step size  $\Delta a\mu_q$ <sup>1</sup> in order to find  $\mu_q = \mu_L(T)$ <sup>2</sup> and the respective densities  $n_{B,L}^{(1)}$  and  $n_{B,L}^{(2)}$  at which the probability is maximal. This is done for temperatures in the range  $[0.4, 0.92]$ , where for each temperature the DoS is sampled for the volumes  $V = 4^3, 6^3$  and  $8^3$ . For temperature  $aT = 0.95$  we have a chosen larger volume set ( $V = 8^3, 10^3$  and  $12^3$ ) since the peak locations for volumes smaller than  $V = 8^3$  becomes ambiguous.

In order to obtain information about the accuracy of the Wang-Landau method we can extract the pseudocritical points for various simulations of  $g(B, T)$  and compute the resulting statistical error. The accuracy control parameters used and the statistical error for yielding the pseudocritical points are shown in Tab. 5.1. Since the error for yielding  $a\mu_L(T)$  is of magnitude  $\sim 10^{-4} - 10^{-5}$ , it is reasonable to choose a step size not smaller than  $\Delta a\mu_L = 10^{-5}$  for finding the pseudocritical point.

<sup>1</sup>Note that we can find the  $a\mu_L(T)$  with arbitrary high precision since we can evaluate the exact expression (5.2).

<sup>2</sup>We started from some reasonable close  $a\mu_q$  and used the step size to approach  $a\mu_L$ . While observing the maxima, we have found the best approximation for  $a\mu_L$  when the maxima location performs a sudden jump.

$aT$	$L$	$\delta/\bar{H}$	$f_{final}$	$\epsilon(a\mu_L(T))$	$\epsilon(n_{B,L}^{(1)}(T))$	$\epsilon(n_{B,L}^{(2)}(T))$
	4	0.1	10e-07	5.1e-04	2.1e-04	5.2e-04
0.4	6	0.15	10e-07	4.9e-04	3.3e-03	2.3e-03
	8	0.2	10e-05	3.5e-03	1.7e-03	1.7e-3
	4	0.05	10e-08	2.8e-04	0	1.4e-03
0.5	6	0.1	10e-08	7.7e-05	1.4e-03	4.4e-04
	8	0.15	10e-07	0 e	0	4.9e-04
	4	0.05	10e-08	2.0e-04	0	2.8e-03
0.6	6	0.1	10e-08	6.7e-05	8.3e-04	8.3e-04
	8	0.15	10e-08	3.2e-05	6.2e-04	9.3e-04
	4	0.05	10e-08	5.6e-05	0	0
0.7	6	0.1	10e-08	3.8e-05	0	0
	8	0.15	10e-08	3.0e-05	6.2e-04	0
	4	0.05	10e-08	8.7e-05	7.8e-03	0
0.8	6	0.1	10e-08	1.0e-04	1.9e-03	8.3e-04
	8	0.15	10e-08	3.1e-05	6.2e-04	9.3e-04
	4	0.05	10e-08	2.1e-04	7.8e-03	0
0.92	6	0.1	10e-08	1.9e-04	4.6e-03	2.7e-03
	8	0.15	10e-08	1.6e-05	2.1e-03	1.3e-03
	8	0.15	10e-07	2.2e-05	5.1e-03	4.9e-03
0.95	10	0.2	10e-07	1.4e-04	1.2e-03	8.4e-03
	12	0.3	10e-06	4.0e-04	1.4e-02	4.8e-02

TABLE 5.1: Accuracy control parameters and statistical errors  $\epsilon$  obtained for the pseudocritical points  $n_{B,L}^{(1)}(T)$ ,  $n_{B,L}^{(2)}(T)$  and  $a\mu_L(T)$  for temperatures  $0.4 \leq aT \leq 0.95$ . The data is obtained by evaluating the probability distribution (Eq. 5.2) using the DoS generated via the Wang-Landau method in a MDP-CT system, where for the statistical error 10 simulations for  $g(P, T)$  were done. The peak locations may sometimes coincide for all simulations with the same  $V$  and  $aT$  which results in zero error.

The results for the probability distribution at  $a\mu_L(T)$ , admitting the double peak structure, are shown for different volumes and for temperatures below  $aT \approx 1.0$  in Fig. 5.5.<sup>3</sup>

Having identified the pseudocritical points for various lattice volumes we can now apply finite size scaling in order to get the critical points  $a\mu_c(T)$ ,  $n_{B,c}^{(1)}(T)$  and  $n_{B,c}^{(2)}(T)$  at  $aT$ . The respective fitting functions are of the form

$$a\mu_L = a\mu_c + CL^{-3} \quad , \quad n_{B,L} = n_{B,c} + \tilde{C}L^{-1} \quad (5.3)$$

with coefficients  $C$  and  $\tilde{C}$ . In Fig. 5.9, the resulting weighted fit for  $a\mu_c$ ,  $n_{B,c}^{(1)}$  and  $n_{B,c}^{(2)}$  is explicitly shown for temperatures within  $[0.5, 0.95]$ .

<sup>3</sup>Considering the intermediate part of the distribution for temperature  $aT = 0.7$  in Fig. 5.5 we find that the probability already decreases down to  $10^{-8}$  which is the reason why conventional Monte Carlo algorithms become unfeasible when approaching  $a\mu_L(T)$ .

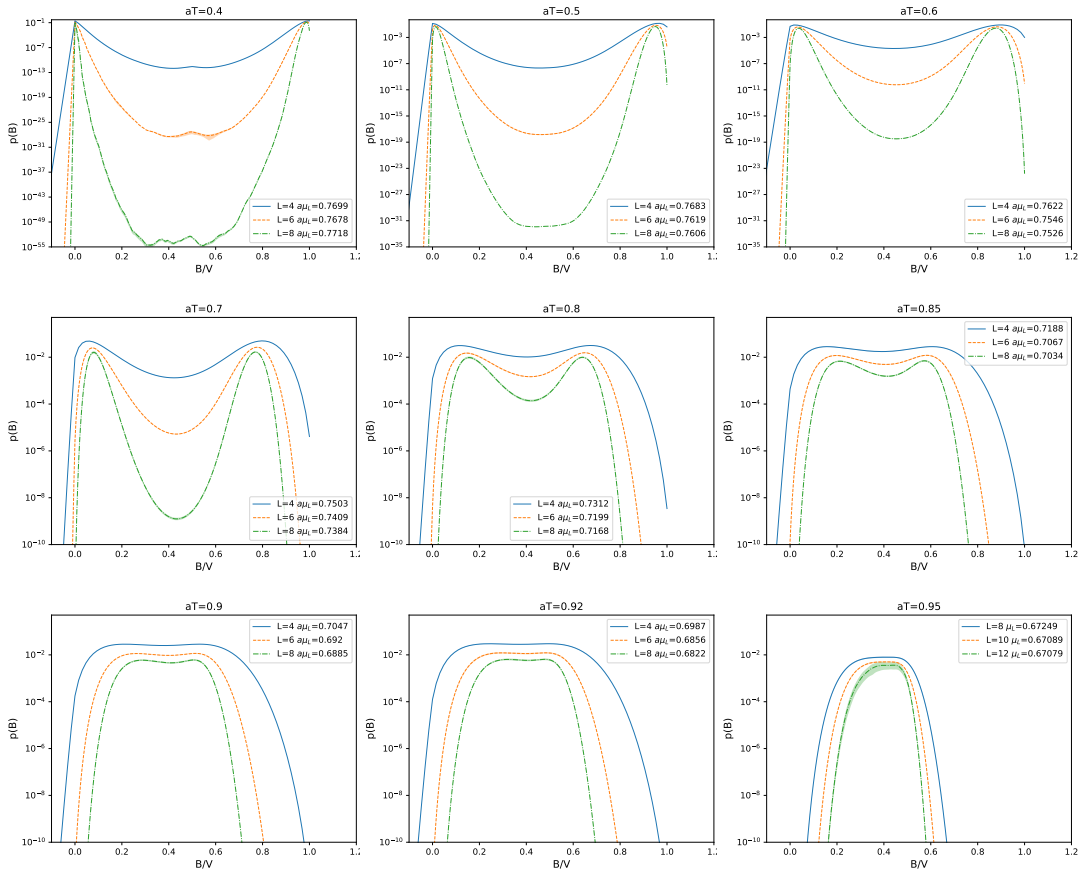


FIGURE 5.5: Grand canonical probability distribution  $p(\mu_L, T, B)$  (Eq. 5.2) at  $a\mu_L(T)$  for temperature  $0.4 \leq aT \leq 0.95$ , where for each  $aT$  we evaluated  $p(\mu_L, T, B)$  for the spatial extents  $L = 4, 6$  and  $L = 8$ .

Performing the extrapolation (weighted fit of Eqs. 5.3) using  $a\mu_L(T)$ , the transition line  $a\mu_c(T)$  in the thermodynamic limit (see solid line in the top of Fig. 5.6) can be identified. Additionally extrapolating the peak locations  $n_{B,L}^{(1)}$  and  $n_{B,L}^{(2)}$ , we get the boundary of the coexistence phase (see the solid line in the bottom of Fig. 5.6). Note, in the cross-over region we used  $a\mu_c(T)$  obtained by measuring chiral observables [4] at the second order phase transition. In order to obtain  $n_{B,L}(T)$  (no more double peak) at the cross-over, we inserted  $a\mu_c(T)$  into the probability distribution Eq. (5.2), where the DoS was generated for the according temperatures. Performing the extrapolation using  $n_{B,L}(T)$  for different volumes, we get  $n_{B,c}(T)$  at the cross-over region.

To obtain the canonical phase diagram with respect to the polymer number  $P$ , hence in the  $T - n_p$  plane, the steps above are repeated using the probability distribution

$$p(\mu_q, T, P) = g(P, T) (2 \cosh(3\mu_q/T))^P / \mathcal{Z}(\mu_q, T) \quad . \quad (5.4)$$

The corresponding double peak structure at  $a\mu_L(T)$  at the nuclear transition is displayed in Fig. 5.7. Extrapolating once again, we get the profile for the coexistence region in the  $T - n_p$  plane shown in Fig. 5.8 and Tab. 5.2.

The obtained data for the critical points for  $B$  and  $P$  is additionally listed in Tab. 5.2.

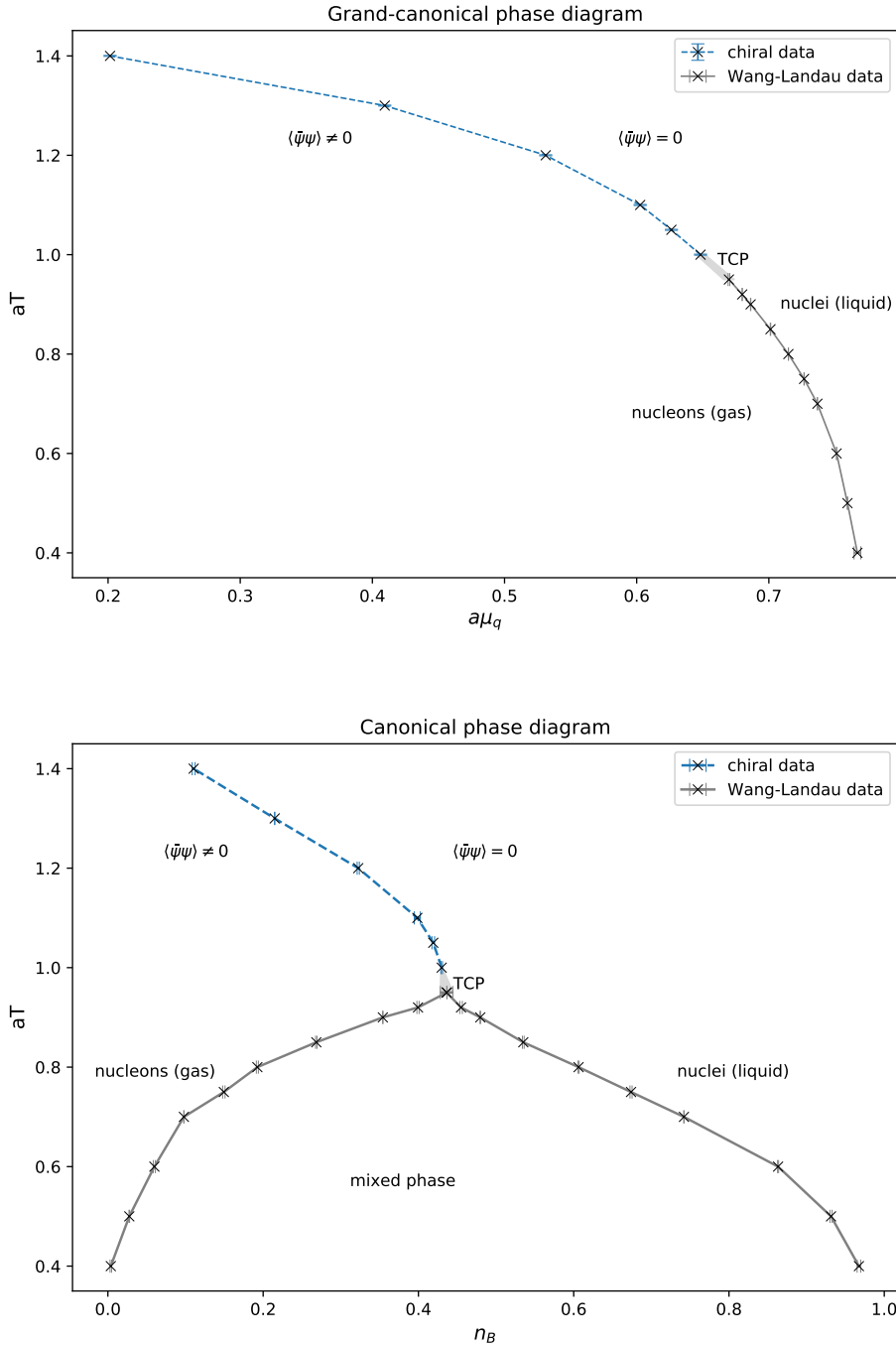


FIGURE 5.6: The profile of the grand canonical (top) and canonical (bottom, in the baryon density  $n_B = B/V$ ) phase diagram for continuous time lattice SC-QCD in the thermodynamic limit, obtained from the Wang-Landau method (solid line). Above  $aT \approx 1.0$  the data (dashed line) is obtained by measuring the chiral susceptibility at the second order transition, where additional simulations for the DoS are necessary to determine the peak locations. The shaded areas within  $[0.95, 1.0]$  denotes location where the tricritical point (TCP) is expected.

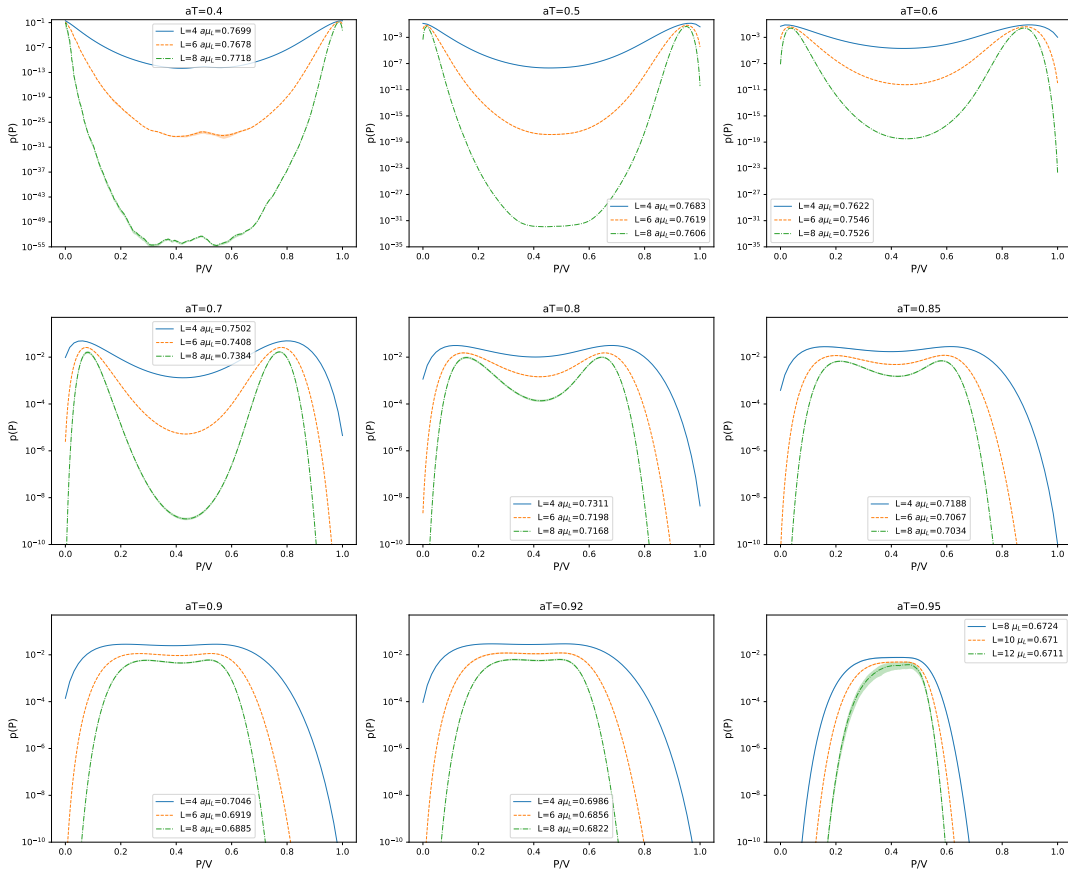


FIGURE 5.7: Grand canonical probability distribution  $p(\mu_L, T, P)$  (Eq. 5.4) at  $a\mu_L(T)$  for temperature  $0.4 \leq aT \leq 0.95$ , where for each  $aT$  we evaluated  $p(\mu_L, T, P)$  for the spatial extents  $L = 4, 6$  and  $L = 8$ .

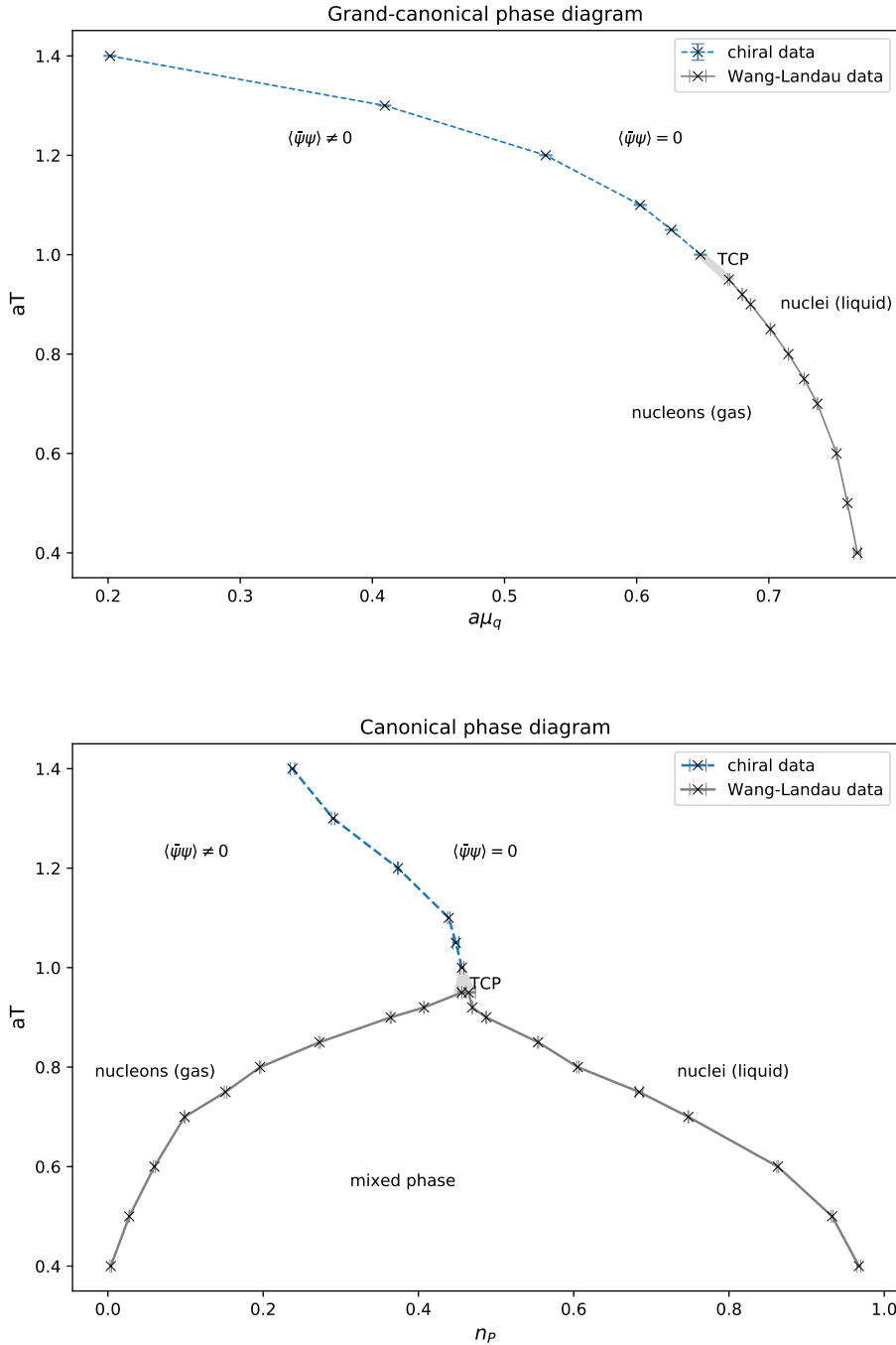


FIGURE 5.8: The profile of the grand canonical (top) and canonical (bottom, in the polymer density  $n_p = P/V$ ) phase diagram for continuous time lattice SC-QCD in the thermodynamic limit, obtained from the Wang-Landau method (solid line). Above  $aT \approx 1.0$  the data (dashed line) is obtained by measuring the chiral susceptibility at the second order transition, where additional simulations for the DoS are necessary to determine the peak locations. The shaded areas within  $[0.95, 1.0]$  denotes location where the tricritical point (TCP) is expected.

$aT$	$a\mu_c$	$n_{B,c}^{(1)}$	$n_{B,c}^{(2)}$
0.4	$0.767 \pm 0.002$	$0.0037 \pm 0.0009$	$0.967 \pm 0.002$
0.5	$0.7594 \pm 0.0001$	$0.0275 \pm 0.0003$	$0.931 \pm 0.001$
0.6	$0.75125 \pm 0.00004$	$0.059 \pm 0.001$	$0.8632 \pm 0.0006$
0.7	$0.73674 \pm 0.00004$	$0.0979 \pm 0.0001$	$0.741 \pm 0.003$
0.75	$0.7266 \pm 0.0001$	$0.149 \pm 0.001$	$0.675 \pm 0.001$
0.8	$0.71478 \pm 0.00008$	$0.192 \pm 0.001$	$0.6062 \pm 0.0007$
0.85	$0.7012 \pm 0.0001$	$0.2685 \pm 0.0009$	$0.535 \pm 0.001$
0.9	$0.6862 \pm 0.0001$	$0.3535 \pm 0.0001$	$0.4796 \pm 0.0003$
0.92	$0.67984 \pm 0.00006$	$0.399 \pm 0.001$	$0.455 \pm 0.001$
0.95	$0.669 \pm 0.001$	$0.415 \pm 0.001$	$0.454 \pm 0.004$

$aT$	$a\mu_c$	$n_{P,c}^{(1)}$	$n_{P,c}^{(2)}$
0.4	$0.767 \pm 0.002$	$0.0037 \pm 0.0009$	$0.967 \pm 0.003$
0.5	$0.7594 \pm 0.0001$	$0.0275 \pm 0.0003$	$0.932 \pm 0.001$
0.6	$0.75125 \pm 0.00004$	$0.059 \pm 0.001$	$0.862 \pm 0.001$
0.7	$0.73674 \pm 0.00004$	$0.0988 \pm 0.0004$	$0.7476 \pm 0.0006$
0.75	$0.7266 \pm 0.0001$	$0.1514 \pm 0.001$	$0.684 \pm 0.005$
0.8	$0.71479 \pm 0.00008$	$0.1961 \pm 0.0008$	$0.605 \pm 0.001$
0.85	$0.7012 \pm 0.0001$	$0.272 \pm 0.001$	$0.5542 \pm 0.0006$
0.9	$0.6862 \pm 0.0001$	$0.3634 \pm 0.0003$	$0.4873 \pm 0.0007$
0.92	$0.67985 \pm 0.00007$	$0.4071 \pm 0.0004$	$0.4693 \pm 0.0003$
0.95	$0.669 \pm 0.001$	$0.455 \pm 0.004$	$0.464 \pm 0.008$

TABLE 5.2: Results for the critical points  $a\mu_c$ ,  $n_{B/P,c}^{(1)}$  and  $n_{B/P,c}^{(2)}$  in the thermodynamic limit of continuous time SC-LQCD from the Wang-Landau method. The error is obtained by calculation of the residuals which reflects the quality of the weighted fit.

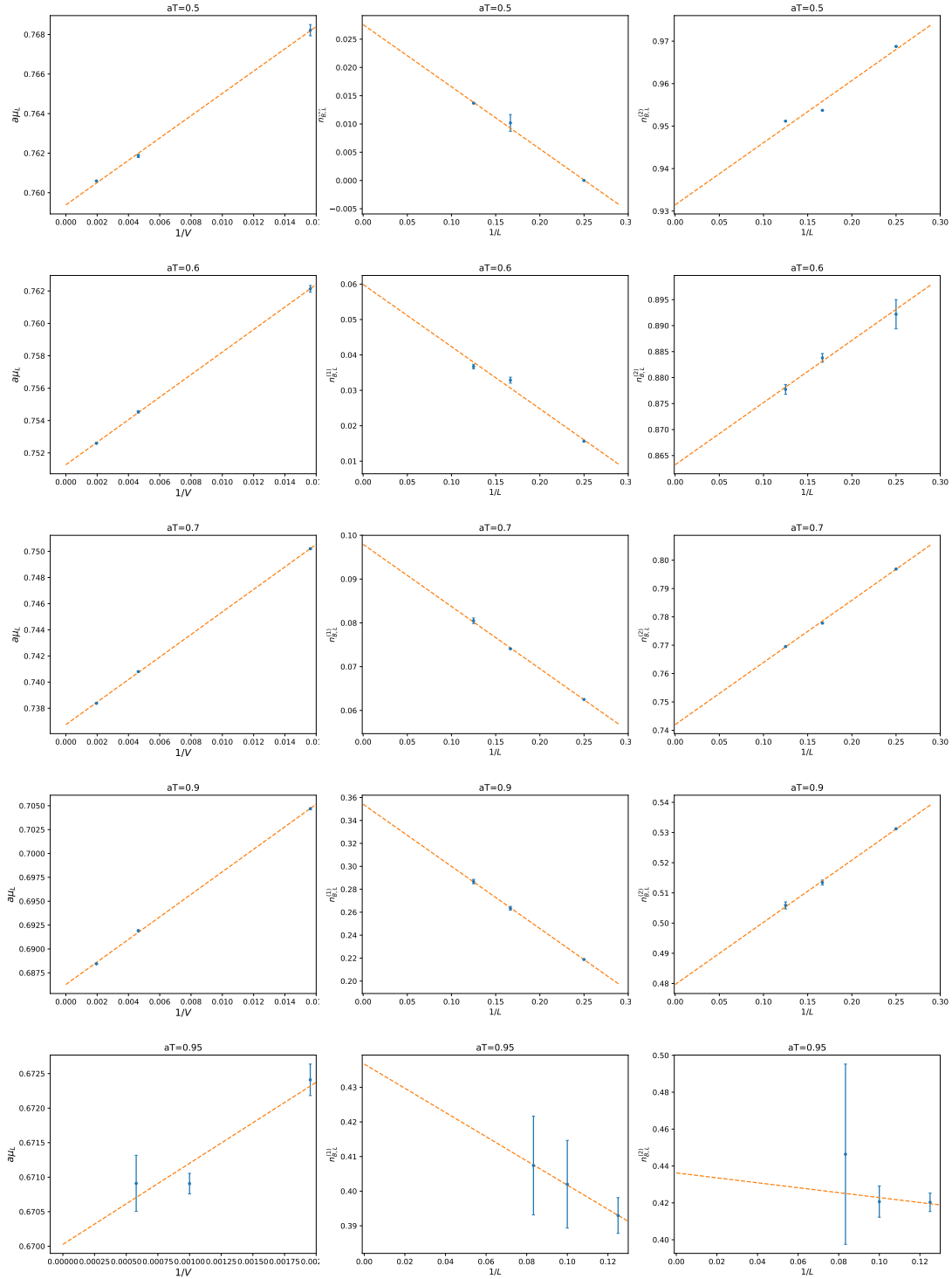


FIGURE 5.9: Fits for finite size scaling to obtain the critical points  $n_{B,c}^{(1)}(T)$ ,  $n_{B,c}^{(2)}(T)$  and  $a\mu_c(T)$  for temperatures in  $[0.5, 0.95]$  in the limit  $V \rightarrow \infty$  of continuous time lattice SC-QCD using the fitting functions (5.3), where each fit is weighted with respect to the statistical error yielded for various simulations.



## Chapter 6

# Discussion and Outlook

We introduced a new method within the continuous time SC-QCD framework. With this method at hand we studied the phase boundary in the grand canonical and canonical diagram, respectively. Our results are shown in Fig. 5.6 and Fig. 5.8, where we performed the thermodynamic limit  $V \rightarrow \infty$ .

The simulations were done for temperatures  $aT \in [0.4, 0.95]$ , where we obtained the DoS for the baryon number  $B = B^+ - B^-$  and the polymer resummation  $P = B^+ + B^-$ . Note that this approach is still impeded by the problem that computational effort increases with decreasing temperature. The reason is that the mesonic worm has to propagate increasingly longer for small  $P$  (or  $B$ ) within the lattice when the temperature becomes small.<sup>1</sup>

Furthermore, our diagram is extended for temperatures at the cross-over using data from chiral observables [4], where the transition to our data near the tricritical point appears to be consistent. However, near  $aT \approx 0.95$ , the error becomes large due to the fact that the double peak structure becomes difficult to detect on the volumes used. Thus, finding the correct peak locations becomes numerical demanding but still possible when choosing larger lattice volumes. We can also observe that for decreasing temperature the left and right phase boundary of the canonical diagram approaches the values  $n_c^{(1)} = 0$  and  $n_c^{(2)} = 1$ , respectively. This agrees with the Silver Blaze phenomenon which states that at  $aT = 0$  thermodynamic observables are independent of  $\mu_q$  up to a critical value  $\mu_c$  [18].

Up to some small deviation we can argue that our results for the phase boundaries for both the canonical and grand canonical diagram are representative for the boundaries of a discrete time system which also involves dynamic baryons. The deviation is small because baryons are heavy and large fluctuations in spatial direction within configurations are rare.

In this thesis we determined the profile of the canonical phase diagram in the strong coupling and chiral limit of LQCD. However, we are interested in weaker couplings and finite quark masses. Hence, future studies may comprise  $\beta$ -corrections which is done by including plaquette contributions from the gauge action before integrating out the gauge fields [19]. By adapting the Wang-Landau method to a discrete time system (see appendix C), it is possible to incorporate finite  $\beta$  and finite quark mass corrections.

---

<sup>1</sup>For future investigations it is highly recommended to perform the Wang-Landau in a parallel fashion as mentioned in Sec. 4.1, when going to smaller temperatures. Especially, when the baryon number approaches zero, we suggest to pick ranges as small as possible.



## Appendix A

# One-link integral for $N_f = 1$

Following the arguments of [4] we first rewrite the one-link integral from Eq. (3.4) into a more compact form

$$\begin{aligned} z(x, \mu) &= \int dU_\mu(x) \exp \left( \eta_\mu(x) \left( \bar{\chi}(x) U_\mu(x) \chi(x + \hat{\mu}) - \bar{\chi}(x + \hat{\mu}) U_\mu(x)^\dagger \chi(x) \right) \right) \\ &\equiv \int_{SU(N_c)} dU_\mu(x) \exp \left( \eta_\mu(x) \text{tr}[Um^\dagger + mU^\dagger] \right) . \end{aligned} \quad (\text{A.1})$$

The matrix  $m$  is  $(m)_{i,j} \equiv \chi_i(x) \bar{\chi}_j(y)$ , writing out the color indices  $i, j = 1, \dots, N$  explicitly. The position  $y$  is related to  $x$  by  $y = x + \hat{\mu}$ . For simplicity we will omit the factor  $\eta_{\hat{\mu}}(x)$  in further calculations.

The fermionic action Eq. (3.2) is invariant under the gauge transformations

$$\chi(x) \rightarrow \Omega(x) \chi(x) \quad \wedge \quad \bar{\chi}(x) \rightarrow \bar{\chi}(x) \Omega(x)^\dagger \quad \text{for } \Omega(x) \in SU(N_c) \quad ,$$

In addition, we know from chapter 3 in [7] that the *Haar measure*  $dU$  is likewise left and right invariant under  $SU(N_c)$  transformations. Thus, the one-link integral  $z(x, \mu)$  itself is gauge invariant and could be expressed as a function of gauge invariant objects of the form  $\text{tr}[mm^\dagger], \dots, \text{tr}[(mm^\dagger)^k], \det[m]$  and  $\det[m^\dagger]$  for  $k \in \mathbb{N}_+$ . Furthermore, every term  $\text{tr}[(mm^\dagger)^k]$  with  $k \geq N_c$  could be written as a combination of expressions  $\text{tr}[mm^\dagger], \dots, \text{tr}[(mm^\dagger)^i], \det[m]$  and  $\det[m^\dagger]$  for  $i < N_c$  using the *Caley-Hamilton theorem* which states: Given any invertible matrix  $A$  of size  $N \times N$  and the characteristic polynomial  $p_c(\lambda) = \det[A - \lambda \mathbb{1}]$  we have  $p_c(A) = 0$ .

Now, we are left with  $N + 1$  gauge invariant expressions, and hence the one-link integral can be expanded into

$$z(x, \mu) = \sum_{k_1, \dots, k_{N+1}} a_{k_1, \dots, k_{N+1}} \det[m]^{k_1} \det[m^\dagger]^{k_2} \text{tr}[mm^\dagger]^{k_3} \cdot \dots \cdot \text{tr}[(mm^\dagger)^{N-1}]^{k_{N+1}} . \quad (\text{A.2})$$

Due to the nilpotency of the Grassmann variables  $\chi$  and  $\bar{\chi}$ , the summation in Eq. (A.2) is limited to  $N_c$  and for the determinants  $\det[m]$  and  $\det[m^\dagger]$  we have separate terms. Thus,

$$\begin{aligned} z(x, \mu) &= \sum_{k=0}^{N_c} \left\{ \alpha_k \text{tr}[(mm^\dagger)^k] \right\} + a \det[m] + b \det[m^\dagger] \\ &\equiv \sum_{k=0}^{N_c} \left\{ \alpha_k (M(x)M(y))^k \right\} + a (-1)^{N_c} N_c! \bar{B}(y)B(x) + b N_c! \bar{B}(x)B(y) , \end{aligned} \quad (\text{A.3})$$

where we removed the trace notation by defining

$$\begin{aligned} \text{tr}[mm^\dagger] &= \chi_i(x)\bar{\chi}_j(y)\chi_j(y)\bar{\chi}_i(x) = \bar{\chi}_i(x)\chi_i(x)\bar{\chi}_j(y)\chi_j(y) \\ &\equiv M(x)M(y) \quad . \end{aligned}$$

Further, we get rid of the determinant notation by writing out the definition explicitly and defining as follows

$$\begin{aligned} \det[m] &= \epsilon_{i_1, \dots, i_{N_c}} m_{1, i_1} \cdots m_{N_c, i_{N_c}} = \frac{1}{N_c!} \epsilon_{i_1, \dots, i_{N_c}} \epsilon_{j_1, \dots, j_{N_c}} m_{i_1, j_1} \cdots m_{i_{N_c}, j_{N_c}} \\ &\equiv (-1)^{N_c} N_c! \bar{B}(y)B(x) \\ \det[m^\dagger] &= N_c! \bar{B}(x)B(y) \quad , \end{aligned}$$

where we have set

$$B(x) \equiv \frac{1}{N_c!} \epsilon_{i_1, \dots, i_{N_c}} \chi_{i_1}(x) \cdots \chi_{i_{N_c}}(x) \quad \text{and} \quad \bar{B}(x) \equiv \frac{1}{N_c!} \epsilon_{i_1, \dots, i_{N_c}} \bar{\chi}_{i_{N_c}}(x) \cdots \bar{\chi}_{i_1}(x) \quad .$$

To determine the coefficients  $a$  and  $b$  we compare Eq.(A.3) with the series expansion of Eq.(A.1),

$$z(x, \mu) = \sum_{k, \ell} \frac{1}{k! \ell!} \int_{SU(N_c)} dU \left( \bar{\chi}(x)U\chi(y) \right)^k \left( -\bar{\chi}(x)U^\dagger\chi(x) \right)^\ell \quad .$$

Terms of the form  $\sim \bar{B}(x)B(y)$  are generated by the summands  $k = N_c$  and  $\ell = 0$ , and thus we have the equality

$$\begin{aligned} b \bar{B}(x)B(y)N_c! &= \frac{1}{N_c!} \int_{SU(N_c)} dU \left( \bar{\chi}(x)U\chi(y) \right)^{N_c} \\ &= \frac{1}{N_c!} \sum_{i_1 \dots i_{N_c}} \sum_{j_1 \dots j_{N_c}} \int_{SU(N_c)} dU U_{i_1, j_1} \cdots U_{i_{N_c}, j_{N_c}} \\ &\stackrel{\text{A.5}}{=} \frac{1}{N_c! N_c!} \sum_{i_1 \dots i_{N_c}} \sum_{j_1 \dots j_{N_c}} \epsilon_{i_1 \dots i_{N_c}} \epsilon_{j_1 \dots j_{N_c}} \bar{\chi}_{i_1}(x) \chi_{j_1}(y) \cdots \bar{\chi}_{i_{N_c}}(x) \chi_{j_{N_c}}(y) \\ &= \bar{B}(x)B(y) \quad , \end{aligned} \tag{A.4}$$

where in the penultimate step we performed the  $SU(N_c)$  integration using

$$\int_{SU(N_c)} dU U_{i_1, j_1} \cdots U_{i_{N_c}, j_{N_c}} = \frac{1}{N_c!} \epsilon_{i_1 \dots i_{N_c}} \epsilon_{j_1 \dots j_{N_c}} \tag{A.5}$$

derived in section 3.1.3 in [7]. From Eq.(A.4) we conclude that  $b = a = 1/N_c!$ . To determine the coefficients  $\alpha_k$  we integrate Eq.(A.1) and Eq.(A.3) over  $\chi(x)$  and  $\bar{\chi}(x)$  with the extra factor  $e^{\bar{\chi}(x)\chi(x)}$ :

$$\int d\chi(x) d\bar{\chi}(x) \int dU_\mu e^{\bar{\chi}(x)\chi(x) + \bar{\chi}(x)U_\mu\chi(y) - \bar{\chi}(y)U_\mu^\dagger\chi(x)} = e^{\bar{\chi}(y)\chi(y)}$$

and

$$\int d\chi(x) d\bar{\chi}(x) e^{\bar{\chi}(x)\chi(x)} \sum_{k=0}^{N_c} \left\{ \alpha_k \text{tr}[(mm^\dagger)^k] \right\} = \sum_{\ell=0}^{N_c} \alpha_\ell \frac{N_c!}{(N_c - \ell)!} (\bar{\chi}(y)\chi(y))^\ell \quad .$$

Setting both equations equal and comparing the coefficients we get

$$\alpha_k = \frac{(N_c - k)!}{N_c!k!} .$$

The one-link integral thus becomes

$$z(x, \mu) = \sum_{k=0}^{N_c} \left\{ \frac{(N_c - k)!}{N_c!k!} \left( M(x)M(y) \right)^k \right\} + \bar{B}(x)B(y) + (-1)^{N_c} \bar{B}(y)B(x) . \quad (\text{A.6})$$

for gauge group  $SU(N_c)$ .



## Appendix B

# Analytic high Temperature Cross-check

In this section a cross-check is done for sampled DoS of a MDP-CT system with a spatial volume of size  $V = 4^3$  using analytic limit case solutions.

In the high temperature region the mesonic worm rarely introduces spatial dimers leading to a configuration space merely consisting of static mesons and polymers. Thus for the limit  $T \rightarrow \infty$ , the state density approximates the analytic solution

$$g(P, T \rightarrow \infty) \approx \binom{V}{P} 4^{V-P} \quad , \quad (\text{B.1})$$

where the factor  $N_c + 1 = 4$  accounts for the different mesonic “spin states”. The analytic limit is indicated by the dashed line in Fig. B.1. We can observe that the relative error  $\epsilon(X) = |(X - X_{exact})/X_{exact}|$ , with  $X_{exact} = \log(g(P, \infty))$ , already lies within the statistical error for the temperatures  $aT = 6, 9$ .

For completeness we compare the expected baryon density (5.1), obtained by  $g(P, T)$ , with the analytic solution in the high temperature limit given by

$$\begin{aligned} \langle B/V \rangle &= \frac{T}{V} \frac{\partial}{\partial \mu_B} \ln(\mathcal{Z}(\mu_B, T)) \\ &\underset{T \rightarrow \infty}{\approx} \frac{\sinh(\mu_B/T)}{2 + \cosh(\mu_B/T)} \quad , \end{aligned} \quad (\text{B.2})$$

where we have used that the partition function approaches the analytic solution

$$\begin{aligned} \mathcal{Z}(\mu_B, T) &= \sum_P g(P, T) w(P, \mu_B/T) \\ &\underset{T \rightarrow \infty}{\overset{\text{B.1}}{\approx}} \sum_P \binom{V}{P} 4^{V-P} (2 \cosh(\mu_B/T))^P \\ &= (4 + 2 \cosh(\mu_B/T))^V \quad . \end{aligned}$$

In Fig. B.2, we can observe that for rising temperature our data again coincides with the analytic solution (B.2).

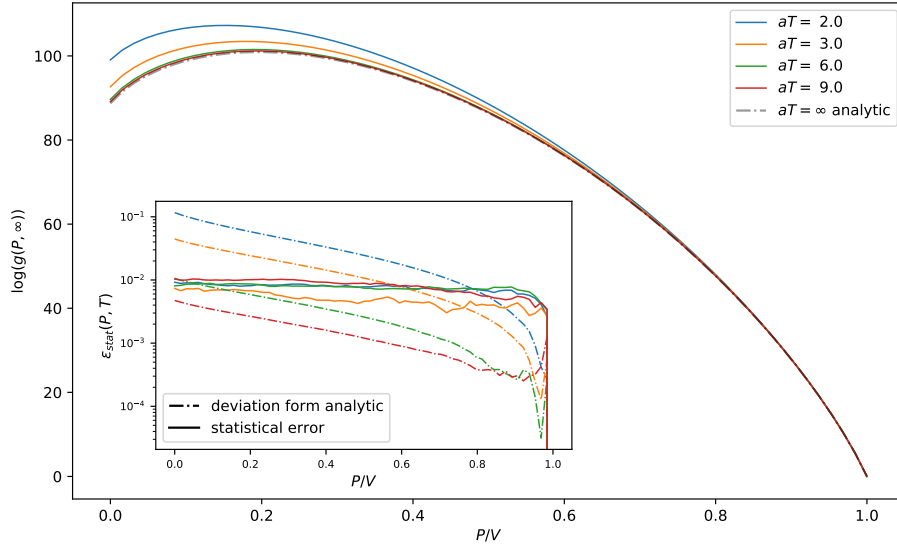


FIGURE B.1: Plot of the results for the density of states of a MDP-CT system of size  $V = 4^3$  for rising temperature, where the dashed line indicates the analytic high temperature solution (B.1). The dashed/solid line in the inset figure shows the deviation/statistical error for the respective temperature.

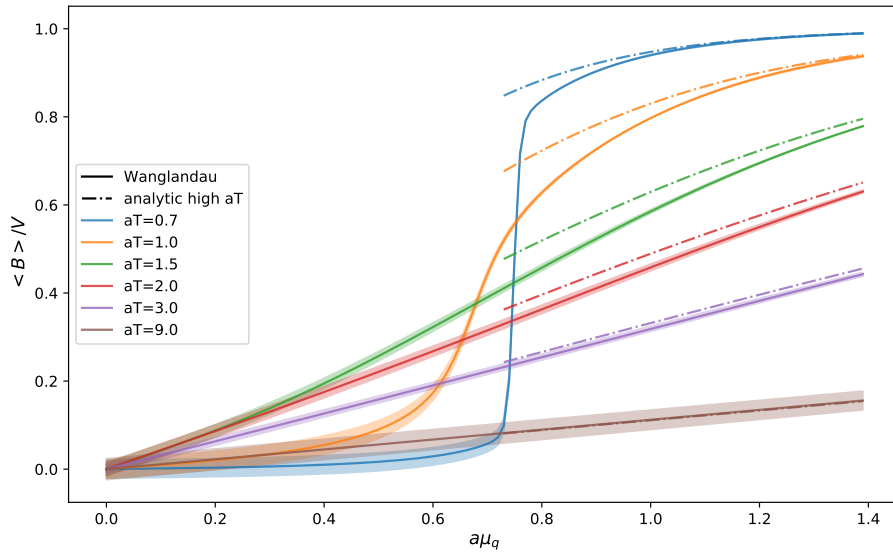


FIGURE B.2: Results for the expectation value of the baryon density (solid lines), obtained by  $g(P, T)$  of a MDP-CT system of size  $V = 4^3$ , for rising temperature. The analytic high temperature solution (B.2) is indicated by the dashed lines.

## Appendix C

# Cross-check with exact data

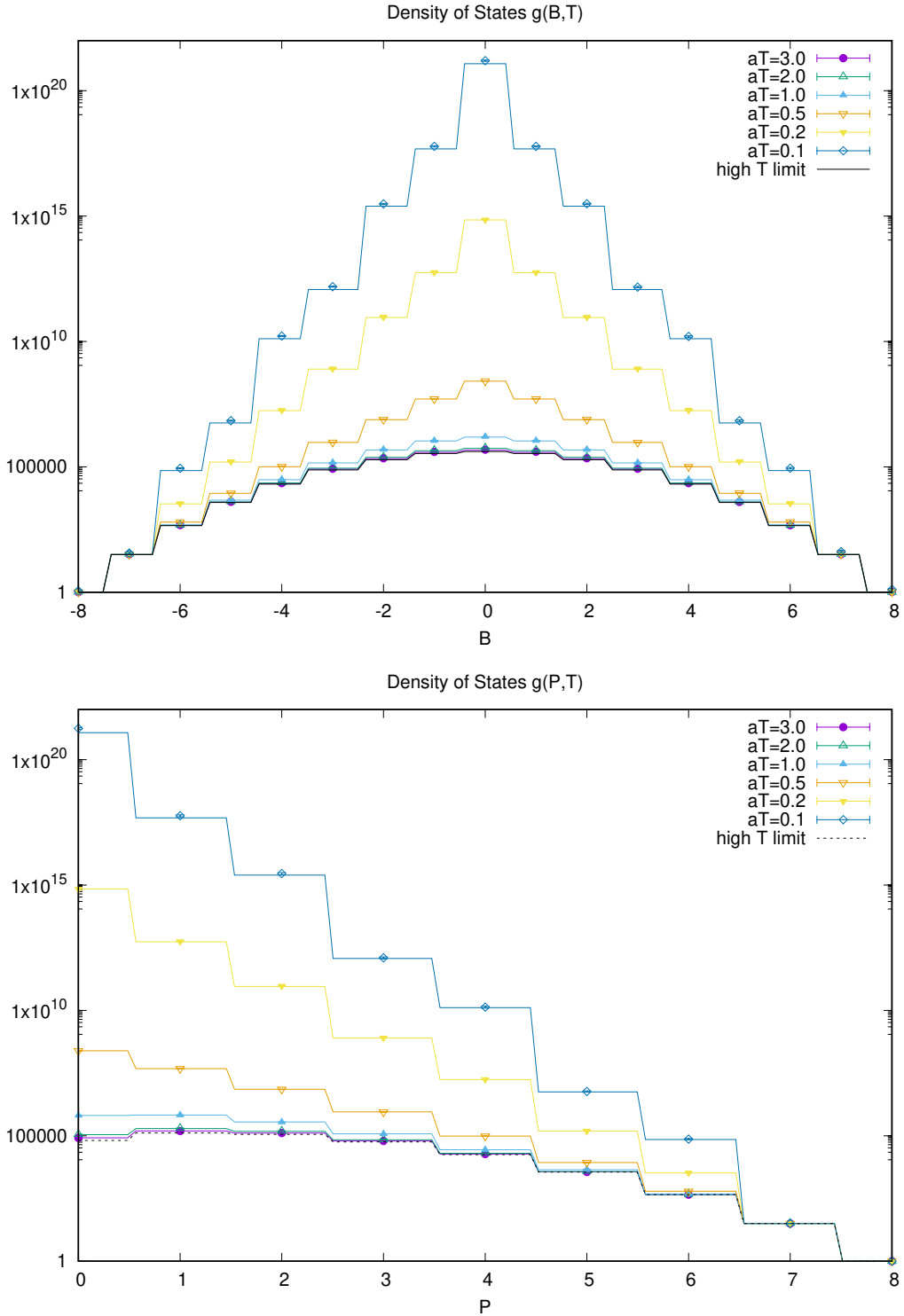
In a MDP system of size  $V = 2^3 \times 2$  it is possible to cross-check the density of states, generated via the Wang-Landau method within a discrete time context, with an exact solution worked out by the Emmy Noether group (J. Kim and W. Unger). Doing so we can get information about the accuracy of the Wang-Landau method.

The Wang-Landau method in a MDP system is implemented in a similar way as in the MDP-CT system. However, in this case we have to exclude dynamic baryons, only allowing baryons to propagate in temporal direction. We then perform mesonic worm updates and subsequently loop through the whole spatial volume, identifying static and dynamic sites and proposing new states for static ones, while immediately accepting dynamic ones.

This approximation, which becomes exact in the continuous time limit, has also only small deviation from the full result for  $N_\tau = 2$ . In the chiral limit, the exact enumeration, mentioned above, employs the following solution for the partition function

$$\begin{aligned} \mathcal{Z}(\mu_q, T) &= \sum_{P=0}^{V_s} \sum_{\kappa=0}^{N_c V} C(\kappa, P) \gamma^\kappa (2 \cosh(\mu_q/T))^P \\ &= \sum_{P=0}^{V_s} g(P, T) (2 \cosh(\mu_q/T))^P \quad , T = \gamma^2/N_\tau \quad , \end{aligned} \quad (\text{C.1})$$

where  $V_s = 2^3$  is the spatial volume, the exponent  $\kappa$  of  $\gamma$  arises from the following summation of the link variables in temporal direction:  $\sum_x (2k_\delta(x) + N_c |b_\delta(x)|)$  (see Eq. 3.9 when taking the chiral limit). The coefficients  $C(\kappa, P)$  are given by the table C.1. Note that  $\kappa$  only takes multiple values of 4. The high temperature result  $g(P, T \rightarrow \infty)$  is in fact identical to the contribution of  $g(P, T)$  from the highest section  $\kappa = 48$ . In Fig. C.1, we can observe that the Wang-Landau data matches with the exact data within the error.



$\kappa \backslash P$	0	1	2	3	4	5	6	7	8
0	8.57e+10	-	-	-	-	-	-	-	-
4	1.0e+10	-	-	-	-	-	-	-	-
8	2.85e+12	-	-	-	-	-	-	-	-
12	3.49e+12	2.16e+10	4.86e+07	-	-	-	-	-	-
16	2.3e+12	6.1e+10	5.03e+08	-	-	-	-	-	-
20	9.29e+11	6.51e+10	1.36e+09	-	-	-	-	-	-
24	2.46e+11	3.7e+11	1.71e+09	-	-	-	-	-	-
28	4.49e+10	1.27e+10	1.17e+09	3.5e+07	5.76e+05	-	-	-	-
32	5.87e+09	2.82e+09	1.17e+08	3.26e+07	9.72e+05	-	-	-	-
36	5.66e+08	4.26e+08	1.19e+08	1.54e+07	9.16e+05	1.88e+04	1.92e+02	-	-
40	4.11e+07	4.51e+07	1.96e+07	4.21e+06	4.62e+05	2.42e+04	5.33e+02	-	-
44	2.18e+06	3.28e+06	2.05e+06	6.83e+05	1.28e+05	1.28e+04	5.33e+02	-	-
48	6.55e+04	1.31e+05	1.15e+05	5.73e+04	1.79e+04	3.58e+03	4.48e+02	3.2e+01	1.0e+00
high aT	6.55e+04	1.31e+05	1.15e+05	5.73e+04	1.79e+04	3.58e+03	4.48e+02	3.2e+01	1.0e+00

TABLE C.1: The coefficients  $C(\kappa, P)$  calculated by Exact enumeration in the Emmy Neether group in order to evaluate the density of states  $g(P, T) = \sum_{\kappa=0}^{N_c V} C(\kappa, P) \gamma^\kappa$  with the bare coupling  $\gamma$ .



# Bibliography

1. Unger, W. & de Forcrand, P. Continuous Time Monte Carlo for Lattice QCD in the Strong Coupling Limit. arXiv:1107.1553, 7 (July 2011).
2. Landau, D, Tsai, S.-H. & Exler, M. A new approach to Monte Carlo simulations in statistical physics: Wang-Landau sampling. *amjph* **72**, 1294 (Oct. 2004).
3. Kratochvila, S. & de Forcrand, P. The canonical approach to Finite Density QCD. **2005** (Oct. 2005).
4. Fromm, M. *Lattice QCD at strong coupling thermodynamics and nuclear physics* Eidgenoessische Technische Hochschule ETH Zuerich. PhD thesis (2010). doi:<https://doi.org/10.3929/ethz-a-006414247>.
5. Shuryak, E. V. *The QCD Vacuum, Hadrons and Superdense Matter* 2nd. doi:10.1142/5367. eprint: <https://www.worldscientific.com/doi/pdf/10.1142/5367>. <https://www.worldscientific.com/doi/abs/10.1142/5367> (WORLD SCIENTIFIC, 2004).
6. Ryder, L. *Quantum Field Theory* 2nd ed. ISBN: 9780521478144. [https://books.google.de/books?id=nnuW\\\_kVJ500C](https://books.google.de/books?id=nnuW\_kVJ500C) (Cambridge University Press, 1996).
7. C. Gattringer, C. B. L. *Quantum Chromodynamics on the Lattice* 1st ed. ISBN: 978-3-642-01849-7. doi:10.1007/978-3-642-01850-3 (Springer, Berlin, Heidelberg, 2010).
8. Montvay, I. & Münster, G. *Quantum Fields on a Lattice* ISBN: 0-521-59917-2. doi:10.1017/CB09780511470783 (Jan. 1997).
9. Hasenfratz, P. & Karsch, F. Chemical potential on the lattice. *Physics Letters B* **125**, 308–310. ISSN: 0370-2693 (1983).
10. Rossi, P. & Wolff, U. Lattice QCD with fermions at strong coupling: A dimer system. *Nuclear Physics B* **248**, 105–122. ISSN: 0550-3213 (1984).
11. Karsch, F. & Mütter, K.-H. Strong coupling QCD at finite baryon-number density. *Nuclear Physics B* **313**, 541–559 (Feb. 1989).
12. De Forcrand, P., Unger, W. & Vairinhos H, e. Strong-coupling lattice QCD on anisotropic lattices. *Phys. Rev. D* **97**. arXiv:1710.00611, 034512 (3 2018).
13. Unger, W. & de Forcrand, P. New algorithms and new results for strong coupling LQCD, 7 (Nov. 2012).
14. De Forcrand, P. *Monte Carlo Algorithms* (lecture 2010).
15. Ferdinand, A. E. & Fisher, M. E. Bounded and Inhomogeneous Ising Models. I. Specific-Heat Anomaly of a Finite Lattice. *Phys. Rev.* **185**, 832–846 (2 Sept. 1969).
16. D. Beale, P. Exact Distribution of Energies in the Two-Dimensional Ising Model. *Physical review letters* **76**, 78–81 (Feb. 1996).
17. Adams, D. H. & Chandrasekharan, S. Chiral limit of strongly coupled lattice gauge theories. *Nuclear Physics B* **662**, 220–246. ISSN: 0550-3213 (2003).

18. Gattringer, C. & Kloiber, T. Lattice study of the Silver Blaze phenomenon for a charged scalar field. *Nuclear Physics B* **869**. doi:[10.1016/j.nuclphysb.2012.12.005](https://doi.org/10.1016/j.nuclphysb.2012.12.005) (June 2012).
19. De Forcrand, P., Philipsen, O. & Unger, W. QCD phase diagram from the lattice at strong coupling (Mar. 2015).